JACS
JOURNAL OF THE AMERICAN CHEMICAL SOCIETY
pubs.acs.org/JACS
Article

When van der Waals Met Kagome: A 2D Antimonide with a Vanadium-Kagome Network

Aishwarya Mantravadi, Bradyn C. Weaver, Shiya Chen, Shahnaz Mukta, Yao Abusa, Arka Sarkar, Yang Sun, Yaroslav Mudryk, Alexander Gundlach-Graham, Kai-Ming Ho, Oleg I. Lebedev, and Julia V. Zaikina*

Cite This: J. Am. Chem. Soc. 2024, 146, 26786−26800
Read Online

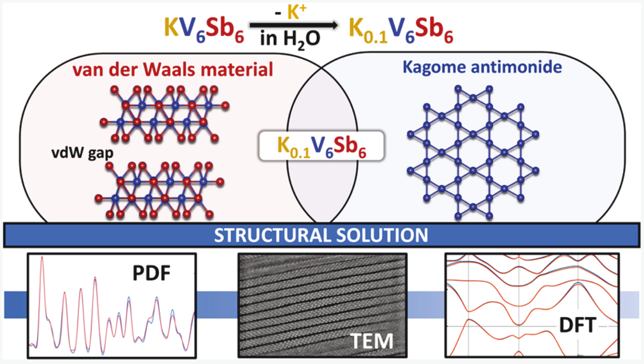

ABSTRACT: 2D materials showcase unconventional properties emerging from quantum confinement effects. In this work, a "soft chemical" route allows for the deintercalation of K^+ from the layered antimonide KV_6Sb_6, resulting in the discovery of a new metastable 2D-Kagome antimonide $K_{0.1(1)}V_6Sb_6$ with a van der Waals gap of 3.2 Å. The structure of $K_{0.1(1)}V_6Sb_6$ was determined via the synergistic techniques, including X-ray pair distribution function analysis, advanced transmission electron microscopy, and density functional theory calculations. The $K_{0.1(1)}V_6Sb_6$ compound crystallizes in the monoclinic space group $C2/m$ (a = 9.57(2) Å, b = 5.502(8) Å, c = 10.23(2) Å, β = 97.6(2)°, Z = 2). The $[V_6Sb_6]$ layers in $K_{0.1(1)}V_6Sb_6$ are retained upon deintercalation and closely resemble the layers in the parent compound, yet deintercalation results in a relative shift of the adjacent $[V_6Sb_6]$ layers. The magnetic properties of the $K_{0.1(1)}V_6Sb_6$ phase in the 2−300 K range are comparable to those of KV_6Sb_6 and another Kagome antimonide KV_3Sb_5, consistent with nearly temperature-independent paramagnetism. Electronic band structure calculation suggests a nontrivial band topology with flat bands and opening of band crossing afforded by deintercalation. Transport property measurements reveal a metallic nature for $K_{0.1(1)}V_6Sb_6$ and a low thermal conductivity of 0.6 W K^{-1} m^{-1} at 300 K. Additionally, ion exchange in KV_6Sb_6 via a solvothermal route leads to a successful partial exchange of K^+ with A^+ (A = Na, Rb, and Cs). This study highlights the tunability of the layered structure of the KV_6Sb_6 compound, providing a rich playground for the realization of new 2D materials.

■ INTRODUCTION

The potential of realizing emergent material properties that arise from the confinement of charge and heat transport to a plane has fueled the quest for two-dimensional (2D) materials.[1,2] As 2D materials possess layered structures, where individual layers are held together by van der Waals (vdW) interactions, they boast electronic, magnetic, thermal, mechanical, and optical properties significantly different from their three-dimensional (3D) analogs.[1,3,4] A notable example is the discovery of unconventional superconductivity in bilayer graphene,[3,4] a 2D analog of non-superconducting graphite.

The motivation to expand the library of 2D materials beyond graphene has led to extensive study of other classes of 2D materials, such as the transition metal dichalcogenides (TMDs) MX_2 (M = transition metal, X = S−Te),[5] *MXenes* derived from *MAX* phases (M = transition metal, A = Al, Si, Ga, X = C or N),[6−8] and, more recently, the boride analogs of *MXenes*, i.e., *MBenes* obtained from *MAB* phases (M = transition metal, A = Al, In, and B = boron).[9,10] TMDs, *MXenes*, and *MBenes* have been explored for many applications, including optoelectronics, energy storage, and catalysis.[5,7−9]

Many of the methods that enable synthesis of the above 2D materials employ low-temperature "soft chemistry" routes.[6,10−19] Reaction pathways in "soft chemistry" methods are oftentimes kinetically controlled, providing access to metastable 2D materials.[20−22] One of the methods used for 2D material synthesis is topochemical deintercalation, which is the selective removal of atoms/ions from a host material while preserving the structural features of the host.[10−14]

While deintercalation of the TMD, *MAX*, and *MAB* phases has been extensively explored, the route remains underexplored for layered compounds within the Kagome class of materials. Structures of Kagome compounds feature a Kagome sublattice, which is a flat network of atoms composed of hexagonal and triangular motifs forming a star-like pat-

Received: May 28, 2024
Revised: September 6, 2024
Accepted: September 9, 2024
Published: September 21, 2024

tern.[23−28] The geometry of the Kagome lattice does not allow for perfect antiferromagnetic alignment of magnetic moments, leading to magnetic frustration. Such structural features render Kagome compounds with distinctive properties, such as superconductivity, Dirac Fermion behavior, quantum spin liquid behavior, and charge density waves.[23−31] In Kagome compounds, the Kagome sublattice can either be a part of a three-dimensional crystal structure like in the $MgCo_6Ge_6$ and ScV_6Sn_6 intermetallics[32,33] or form (bi)layers like in the Fe_3Sn_2 compound.[30,34] There are also examples where the Kagome sublattice is part of covalently bonded layers that are well separated from each other by layers of electropositive cations, such as in $Cs_2Pd_3S_4$ or $CsCu_3S_2$, where the layers containing the Pd/Cu Kagome-net alternate with the Cs layers.[35,36] Although rare, similar layered compounds are found among the pnictides, for instance, the $K_3Cu_3P_2$ phase.[37] For the heavier pnictides (Sb and Bi), the family of layered Kagome compounds was recently extended with the discovery of AV_3Sb_5, AV_6Sb_6 (A = K, Rb, Cs), and ATi_3Bi_5 (A = Rb, Cs) compounds.[26,31,38−43] The layered structure of these new families of compounds, where the Kagome network of transition metals (Ti or V) is well separated by layers of alkali metal cations, makes them suitable candidates for deintercalation studies, such that selective removal of alkali metal cations can pave the way toward the synthesis of new 2D materials while preserving the Kagome net. The exciting physics of 2D materials combined with the unique electronic structures afforded by the Kagome lattice is an attractive pursuit in the discovery of novel 2D materials with emergent properties.[44,45]

Herein, we studied the deintercalation of K^+ from the layered Kagome antimonide KV_6Sb_6, where the $[V_6Sb_6]$ layers are separated by the layers of K^+ cations. A single $[V_6Sb_6]$ layer comprises double layers of $[V_3Sb]$, featuring a Kagome bilayer of V atoms, terminated by a single layer of Sb atoms on either side. Using water, a nearly complete deintercalation of K^+ from KV_6Sb_6 is achieved, leading to the discovery of a new pnictide-based metastable 2D-Kagome material with a vdW gap of 3.2 Å. The crystal structure of the deintercalated product was unveiled by utilizing a synergistic combination of X-ray pair distribution function (PDF) analysis, scanning transmission electron microscopy (STEM), and density functional theory (DFT) calculations, an approach successfully used earlier for atomic structure determination of metastable $Li_{\sim 0.5}NiB$.[11] We investigated the effect of K^+ removal on the low-temperature magnetic and transport properties. Through our work, we provide an example of facile synthesis and strategy for structural determination of new metastable 2D compounds. Such a strategy can be extended toward other layered pnictides to expand the library of novel 2D materials.

■ EXPERIMENTAL SECTION

Synthesis of the deintercalated $K_{0.1(1)}V_6Sb_6$ phase starts with the preparation of the parent KV_6Sb_6 compound using KH, V, and Sb powders, as described in our earlier work,[39] followed by the topotactic deintercalation of K^+ using water. Deintercalation was also attempted using other solvents, such as 0.1 M HCl, methanol, and ethanol. We performed ion exchange experiments with KV_6Sb_6 under nonsolvothermal and solvothermal conditions. The experimental design for the nonsolvothermal ion-exchange reactions was adopted from the work by Manos et al.[46] For the solvothermal ion exchange experiment, KV_6Sb_6, a suitable alkali metal salt, and the desired solvent were placed inside a stainless-steel autoclave with a subsequent reaction in a solvothermal furnace.

The synthesized samples were analyzed by powder X-ray diffraction (PXRD) using a Rigaku MiniFlex600 powder diffractometer with Cu K_α radiation (λ = 1.54051 Å). To determine the K content in the parent KV_6Sb_6 and deintercalated $K_{0.1(1)}V_6Sb_6$ compounds, the samples were analyzed using a nitrogen (N_2)-sustained microwave inductively coupled atmospheric pressure plasma mass spectrometer (MICAP-MS, Analytik Jena, Germany). Operation details and applications of the N_2-MICAP-MS for elemental analysis have been described elsewhere.[47−51]

Total scattering data suitable for PDF analysis were collected at beamline 11 ID-B at the Advanced Photon Source at Argonne National Lab (APS ANL) using λ = 0.1432 Å. The PDF, $G(r)$, was obtained by direct Fourier transformation of scattering structure function $S(Q)$ obtained using the program PDF Suite/PDFgetX3.[52] PDF data were analyzed using the program PDFgui.[53] High-temperature synchrotron PXRD data were collected at synchrotron beamline 17-BM at APS ANL (λ = 0.24089 Å).[54]

Scanning electron microscopy-energy dispersive X-ray analysis (SEM-EDX) was performed using an FEI Quanta 250 field-emission SEM equipped with an Oxford X-Max 80 detector to determine the sample elemental composition. Transmission electron microscopy (TEM), including electron diffraction and high-angle annular dark field (HAADF)-STEM, studies were performed using a JEM ARM200F cold FEG double aberration corrected electron microscope operated at 80 kV/200 kV.

Measurement of magnetic properties was performed using a Quantum Design MPMS XL-7 magnetometer. Transport properties were measured by using the commercial multipurpose Physical Properties Measurement System Evercool I (PPMS, Quantum Design). A PerkinElmer Lambda 1050+ UV/vis/NIR spectrometer equipped with a 150 mm Spectralon-coated integrating sphere was used for the diffuse reflectance measurements.

Crystal structures were optimized by DFT calculations, which were performed using the projector augmented wave[55] method implemented in the VASP code.[56,57] The exchange and correlation energy were treated with the generalized gradient approximation (GGA) and parametrized by the Perdew−Burke−Ernzerhof (PBE) formula.[58] The calculations of full Brillouin-zone electron−phonon coupling (EPC) constant and the superconducting temperature (T_c) were performed based on density functional perturbation theory[59] implemented in the Quantum ESPRESSO code.[60,61]

Further details about the synthesis and characterization methods used in this work can be found in the Supporting Information.

■ RESULTS AND DISCUSSION

Synthesis. Various deintercalation methods have been employed for the synthesis of layered materials, including electrochemical (de)intercalation[19] and various chemical etchants.[11−16] Examples include deintercalation of K^+ from $K_{2x}Mn_xSn_{1-x}S_2$ using I_2/acetonitrile solution[16] and deintercalation of Li^+ from LiNiB by exposing the material to air.[11] In this work, we used DI water for deintercalation of K^+ from the KV_6Sb_6 layered phase. As seen in Figures 1 and S1, deintercalation leads to a product with broad diffraction peaks, suggesting a decrease in particle size or a diminished

https://doi.org/10.1021/jacs.4c07285
J. Am. Chem. Soc. 2024, 146, 26786−26800

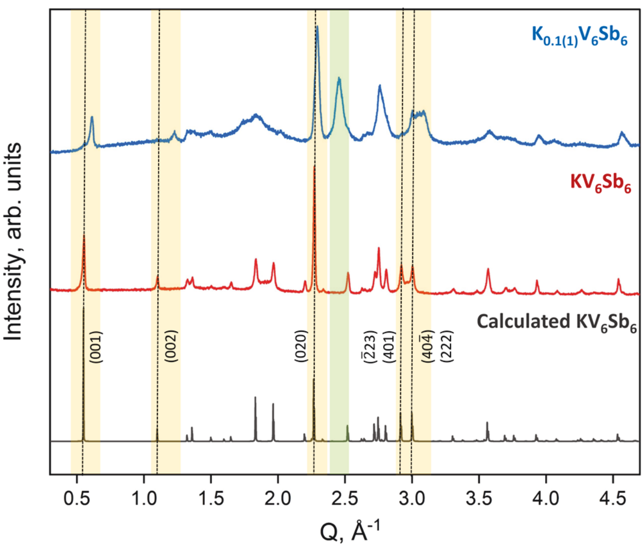

Figure 1. Experimental PXRD patterns for parent KV_6Sb_6 (red) and the deintercalated $K_{0.1(1)}V_6Sb_6$ phase (blue) together with the calculated pattern (black) for the $C2/m$ structure of KV_6Sb_6. Select diffraction peaks (highlighted in yellow) indicate a reduction in unit cell parameters upon deintercalation, while the new diffraction peak (highlighted in green) emerges upon deintercalation. Diffraction peaks are broad, signaling reduced particle size and/or diminished long-range order.

long-range order in the structure. TS1o evaluate the extent of K^+ deintercalation, we used ICP-MS to determine that up to 90(10)% of K^+ can be removed (Table 1). SEM-EDX results (Table 1 and Figure S2) are also consistent with nearly complete K^+ deintercalation, but a higher standard deviation in this method is attributed to the variation in the residual K^+ content from particle to particle. From the results of ICP-MS, we estimated the residual K^+ content in deintercalated samples as 0.1(1); therefore, throughout the text, we will refer to the deintercalated phase as $K_{0.1(1)}V_6Sb_6$. A basic pH of the supernatant after washing with water is likely due to the formation of KOH from the deintercalation of K^+, further supporting the findings of ICP-MS and SEM-EDX.

A qualitative comparison of the PXRD patterns for the parent KV_6Sb_6 compound and the deintercalated product $K_{0.1(1)}V_6Sb_6$ provides insights into the structural change upon deintercalation. The majority of the diffraction peaks for the deintercalated phase are shifted to a higher Q value compared to those for the parent KV_6Sb_6, indicating a reduction in the unit cell size upon removal of K^+ (peaks highlighted in yellow in Figure 1). This includes the (001) peak at $Q \sim 0.5$ $Å^{-1}$ corresponding to the K–K interlayer distance (d = 11.4 Å) in KV_6Sb_6. The similarities in PXRD patterns for the two indicate that the structures of the parent KV_6Sb_6 and the deintercalated phases are related, with possible preservation of certain structural motifs upon deintercalation from KV_6Sb_6. Since ICP-MS and SEM-EDX suggest nearly complete removal of K^+ and a V/Sb ratio close to 1:1 (Table 1), we speculate that the preserved motif is the $[V_6Sb_6]$ layer. Notably, while most of the diffraction peaks are shifted upon deintercalation, an emergence of a new diffraction peak is seen at Q = 2.5 $Å^{-1}$ (highlighted in green in Figure 1), indicating structural variation brought about by deintercalation. A direct reaction of KH, V, and Sb in a 0.2:6:6 molar ratio at 1073 K for 72 h results in the formation of the KV_6Sb_6 phase along with V_3Sb_2. This indicates that the $K_{0.1(1)}V_6Sb_6$ phase can be obtained by deintercalation of K^+ from the parent KV_6Sb_6 compound using the "soft chemistry" route and is most likely metastable.

Other solvents were tried for deintercalation of K^+ from KV_6Sb_6, including an aqueous solution of 0.1 M HCl, methanol (MeOH), and ethanol (EtOH) (Figure S1). The rate of deintercalation of K^+ in 0.1 M HCl (aq) is similar to that in water (nearly complete deintercalation in ~12 h), resulting in the same product based on the comparison of PXRD patterns. The rate of deintercalation of K^+ in MeOH and EtOH is slower, indicated by remnants of diffraction peaks of KV_6Sb_6 and the onset of the characteristic diffraction peak at Q = 2.5 $Å^{-1}$. The PXRD results indicate that a greater extent of deintercalation is achieved in aqueous solutions. Mild effervescence is observed for deintercalation in aqueous solutions, indicating the formation of gaseous products during the process. Comparing the deintercalation of K^+ from KV_6Sb_6 to that in the layered chalcogenide KCo_2Ch_2 (Ch = S, Se),[13] we hypothesize the gaseous product to be H_2 gas.

In addition to testing the deintercalation in different solvents, we also tested the effect of sonication on the rate of deintercalation in water. From PXRD data, sonication of the powder in water results in the same product (Figure S1). We hypothesize that in water and other aqueous media, most of the K^+ is removed instantly during the initial interaction of the KV_6Sb_6 phase with water, followed by subsequent slower removal of the remaining K^+. Hence, sonication does not have a drastic effect on the rate of deintercalation. SEM images in Figure S2 show smaller particle sizes for the sonicated product caused by the breaking of the particles during sonication. The particles of the deintercalated $K_{0.1(1)}V_6Sb_6$ phase display a

Table 1. Elemental Compositions of Parent KV_6Sb_6 and Deintercalated $K_xV_6Sb_6$ Phases Obtained by Using ICP-MS and SEM-EDX to Determine the Extent of K^+ Deintercalation

	KV_6Sb_6	$K_xV_6Sb_6$	LOD (μg/L)	LOQ (μg/L)
K (μg/L)	4.1 ± 0.1	0.3 ± 0.1	0.07	0.24
V (μg/L)	22.9 ± 0.1	31.9 ± 0.3	0.01	0.04
Sb (μg/L)	56.1 ± 0.6	71.1 ± 0.6	0.05	0.16
K/V/Sb from ICP-MS	1.4(1):5.9(1):6.0(1)	0.1(1):6.4(1):6.0(1)		
K/V/Sb from SEM-EDX for $K_xV_6Sb_6$		0.2(1):5.2(1): 6.0(2)[a]		

[a]The composition determined by EDX was averaged from 6 different areas of the sample. The precision in compositional analysis of samples by the EDX method at 1 wt % K is 0.1%, i.e., ~10% relative standard deviation. A greater standard deviation in the estimation of K content from EDX indicates variability in the K content across the sample. The limits of detection (LOD) and limits of quantification (LOQ) for ICP-MS are calculated from calibration plots using 3.0σ/slope and 10.0σ/slope, respectively, where σ is the standard deviation of response (the molar ratios are normalized to 6 Sb atoms per f.u. in KV_6Sb_6).

https://doi.org/10.1021/jacs.4c07285
J. Am. Chem. Soc. 2024, 146, 26786−26800

remarkable layered morphology, not immediately visible in SEM images for the KV_6Sb_6 parent compound (Figure S2).

Overall, the deintercalation of K^+ from the KV_6Sb_6 phase in aqueous solution is facile and fast, leading to the formation of a new metastable $K_{0.1(1)}V_6Sb_6$ phase. $K_{0.1(1)}V_6Sb_6$ displays diminished crystallinity compared to the parent compound, as indicated by the general broadening of the diffraction peaks (Figure 1). PXRD data indicate the preservation of the $[V_6Sb_6]$ layers in the deintercalated product, while a combination of ICP-MS and SEM-EDX suggests nearly complete removal of K^+.

Thermal Stability and Metastability of $K_{0.1(1)}V_6Sb_6$. To determine the thermal stability and confirm the metastability of $K_{0.1(1)}V_6Sb_6$, we collected high-temperature in situ synchrotron PXRD data for a sample of $K_{0.1(1)}V_6Sb_6$ (containing ~10 wt % Sb) sealed into a silica capillary under vacuum. As seen in Figure 2, the $K_{0.1(1)}V_6Sb_6$ phase begins to decompose into stable binary VSb_2 and Sb at a temperature as low as 500 K. The $K_{0.1(1)}V_6Sb_6$ phase continues to decompose on heating and, above 730 K, completely decomposes into VSb_2 and the V_3Sb_2-like intermediate. Further heating to ~1000 K converts the intermediate to stable V_3Sb_2 and VSb_2 binary compounds. Once the two binaries are formed, they remain during the entire cooling cycle, while the $K_{0.1(1)}V_6Sb_6$ phase does not recrystallize upon cooling, further confirming the nearly K-free composition of $K_{0.1(1)}V_6Sb_6$.

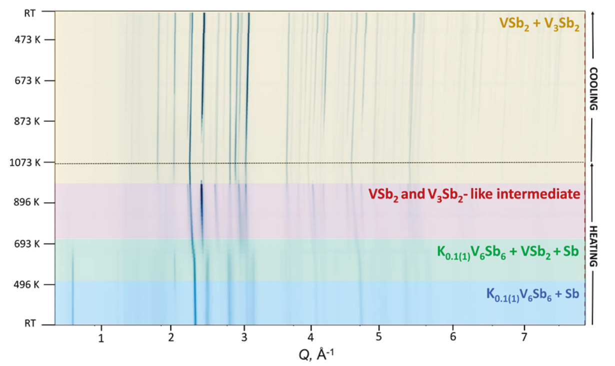

Figure 2. Waterfall diagram representing the high-temperature in situ synchrotron PXRD data for the $K_{0.1(1)}V_6Sb_6$ phase collected upon heating and cooling in a vacuum. The diagram shows sequential changes in PXRD patterns as the sample is heated to 1073 K and cooled to room temperature, where each vertical line represents a diffraction peak in the PXRD pattern. The temperature range with distinct crystalline phases is highlighted in blue, green, red, and yellow. The $K_{0.1(1)}V_6Sb_6$ phase has limited thermal stability and is metastable in nature. In fact, a similar decomposition of $K_{0.1(1)}V_6Sb_6$ to yield Sb is seen during spark plasma sintering (SPS) attempted at 473 K, further supporting that $K_{0.1(1)}V_6Sb_6$ is not stable above 500 K. Figure S3 shows the select PXRD patterns for the in situ PXRD analysis with the diffraction peaks assigned to the crystalline phases formed in temperature ranges highlighted in blue, green, red, and yellow in Figure 2. The above discussion suggests limited thermal stability for $K_{0.1(1)}V_6Sb_6$ and serves as additional proof of the metastability of the $K_{0.1(1)}V_6Sb_6$ phase.

Crystal Structure. The deintercalation of K^+ from KV_6Sb_6 results in the synthesis of the metastable $K_{0.1(1)}V_6Sb_6$ phase, which is thermally unstable, ruling out structural elucidation using single-crystal X-ray diffraction due to the unavailability of single crystals and diminished crystallinity, as seen by PXRD. Hence, we applied a combination of complementary techniques, X-ray PDF analysis, STEM, and DFT calculations, for a thorough and precise structural characterization of the deintercalated compound. This approach was successfully implemented in the past on semicrystalline phases in the Li−Ni−B system obtained via Li^+ deintercalation.[11,62] From PXRD data, similarities between the structures of KV_6Sb_6 and $K_{0.1(1)}V_6Sb_6$ became apparent. Therefore, we examined the structures of both phases using the above strategy to draw a comparison and eventually construct the structural model for the deintercalated $K_{0.1(1)}V_6Sb_6$ phase.

We began with the analysis of the X-ray PDF data for the parent KV_6Sb_6 phase. In our previous work,[39] we determined the $R\bar{3}m$ crystal structure for the KV_6Sb_6 phase using high-resolution PXRD data. During structural determination, the monoclinic $C2/m$ (a = 9.57 Å, b = 5.53 Å, c = 11.87 Å, γ = 105.96°, Z = 2) structure was initially suggested, which upon further analysis with Platon[63] provided the higher symmetry $R\bar{3}m$ model (a = 5.53 Å, c = 34.23 Å, Z = 3), making KV_6Sb_6 isostructural to the RbV_6Sb_6 and CsV_6Sb_6 phases.[40,41] The $R\bar{3}m$ and $C2/m$ models bear close resemblance to one another, except for the splitting of certain diffraction peaks in the PXRD pattern. Due to the broadening of diffraction peaks, such splitting was not observed even in the high-resolution PXRD data; thus, the higher symmetry $R\bar{3}m$ model was proposed for the KV_6Sb_6 phase.[39] Refer to Figure S4 in the SI for a comparison of the two structural models of KV_6Sb_6 and the splitting of the Wyckoff positions associated with transformation from the higher symmetry $R\bar{3}m$ model to the lower symmetry $C2/m$ model. The X-ray PDF data for the parent KV_6Sb_6 phase was analyzed using both $R\bar{3}m$ and $C2/m$ models. Figure 3 shows the fitting of the experimental X-ray PDF data in the r = 2−45 Å range. Both models provide a decent fit, as indicated by the residual curve and refinement parameter R_w (Figure 3a,b). The $C2/m$ model performs better compared to $R\bar{3}m$ as more parameters are refined for the lower symmetry monoclinic space group compared to the rhombohedral one; however, the difference in the quality of the fit is minor (Figure 3). A similar trend is observed for the fit of the PDF data using the $R\bar{3}m$ and $C2/m$ models in the short (r = 2−15 Å), middle (r = 15−30 Å), and long (r = 30−45 Å) ranges, as shown in Figure S5. The above findings suggest the $R\bar{3}m$ model to be a better representation of the structure of the KV_6Sb_6 phase.

As mentioned earlier, a comparison of the PXRD patterns for KV_6Sb_6 and $K_{0.1(1)}V_6Sb_6$ hinted a similar layered structure for the two, with possible retention of the $[V_6Sb_6]$ layers. Intriguingly, the structural similarity is also manifested in the PDF data, as KV_6Sb_6 and $K_{0.1(1)}V_6Sb_6$ have similar $G(r)$ values in the shorter range of r = 2−11 Å (Figure S6a). A similar PDF in the r = 2−11 Å range implies that the atomic interactions in the specified range essentially come from V and Sb atoms in a single $[V_6Sb_6]$ layer and are independent of K, given that the K−K interlayer distance in KV_6Sb_6 is ~11 Å (Figure S6b) and the nearly complete deintercalation of K^+ is observed (Table 1). Pairwise correlations calculated using the $R\bar{3}m$ and $C2/m$ models in the r = 2−16 Å range further support the claim. As seen in Figure S7, the pairwise correlations are comparable for the two structures, with the major contributions from Sb−Sb and V−Sb correlations. The atomic correlations involving the lightest K atom contribute the least to the total PDF and the contribution is nearly zero for the K−K correlation.

Based on these observations, we hypothesized that the refinement of the PDF data for $K_{0.1(1)}V_6Sb_6$ should remain

https://doi.org/10.1021/jacs.4c07285
J. Am. Chem. Soc. 2024, 146, 26786−26800

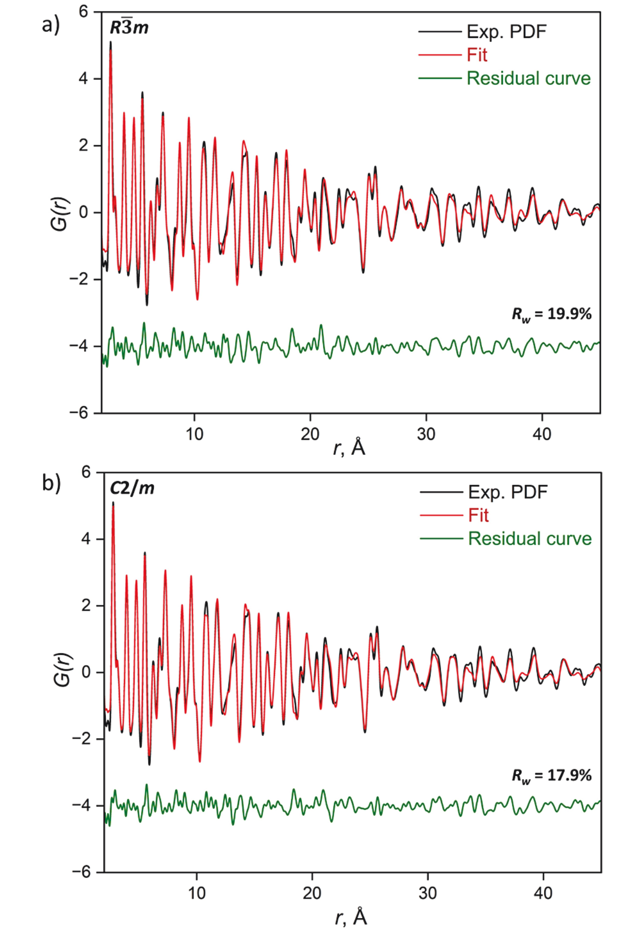

Figure 3. Fitting of the experimental X-ray PDF data in the r = 2−45 Å range for the KV_6Sb_6 phase using the (a) monoclinic model ($C2/m$) and (b) rhombohedral model ($R\bar{3}m$).

unaffected by the presence or absence of K atoms in the structural model. Hence, the fitting of the PDF data for $K_{0.1(1)}V_6Sb_6$ was performed in the r = 2−11 Å range using the $R\bar{3}m$ and $C2/m$ models with 100% K and no K at all. Both models in the $C2/m$ space group (100% and no K) fail to provide a good fit for the PDF data even in the short range (Figure S8). Using the $R\bar{3}m$-based models resulted in an even worse fit of the PDF data. The above PDF analysis pointed to the inadequacies of the current models being used. Therefore, we utilized advanced high-resolution STEM to construct an adequate structural model for the $K_{0.1(1)}V_6Sb_6$ compound.

Figures 4 and 5 show the high-angle annular dark field scanning transmission electron microscopy (HAADF-STEM) images and HAADF-STEM intensity profiles for the KV_6Sb_6 and $K_{0.1(1)}V_6Sb_6$ phases. Figure S9 displays the energy-dispersive X-ray spectra for the two. The HAADF images confirm the layered structures for both KV_6Sb_6 and $K_{0.1(1)}V_6Sb_6$ with similar $[V_6Sb_6]$ layers (Figures 4a and 5a), in excellent agreement with the PXRD and PDF data. Along with retaining the $[V_6Sb_6]$ layers, the hexagonal symmetry of the Sb layers is also preserved (Figures 4e and 5e). Since the intensity in HAADF-STEM images is proportional to $\sim Z^2$ (Z is the atomic number), the wide dark stripes correspond to the layers of lighter K atoms (Figures 4a,c,d and 5a,c,d). The $C2/m$ model allows for the refinement of a greater number of parameters compared to the $R\bar{3}m$ model, hence we used the

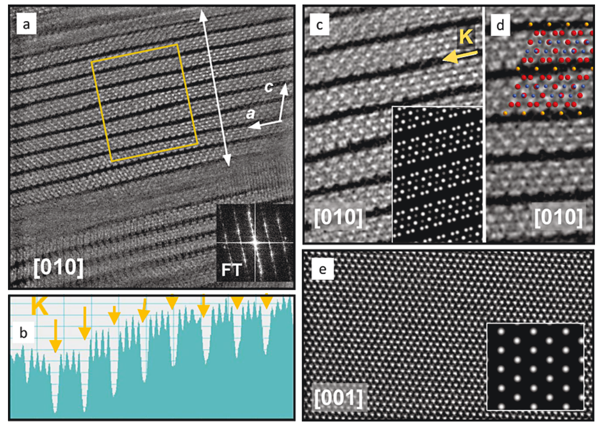

Figure 4. HAADF-STEM data for the KV_6Sb_6 parent phase. (a) HAADF-STEM image along the [010] direction, with the inset showing electron diffraction patterns obtained via fast Fourier transform. The yellow box highlights the variation in thickness of K-layers, signifying areas with denser packing within the K-monolayers. (b) Intensity scan line profiles measured along the line shown with a white double-head arrow in panel (a). (c) Magnified HAADF-STEM image displaying the layered crystal structure. Inset: simulated HAADF-STEM image based on the $C2/m$ model showing a good match to the experimental one. (d) STEM image together with the KV_6Sb_6 $C2/m$ structure overlaid (K: yellow, V: blue, Sb: red spheres). (e) [001] HAADF-STEM image showing a hexagonal symmetry of Sb atoms along the [001] direction. The simulated image is given as an inset.

$C2/m$ model of KV_6Sb_6 as the basis for the analysis of $K_{0.1(1)}V_6Sb_6$ structure.

For the parent KV_6Sb_6 phase, the simulated images using the $C2/m$ model fit exceptionally well with HAADF-STEM images along the [010] direction (Figure 4d). The intensity scan line profile (Figure 4b) along the stacking direction of $[V_6Sb_6]$ layers (shown by the white arrow in Figure 4a) reveals a periodic variation in STEM intensity and, together with the TEM-EDX spectrum (Figure S9), confirms that dark stripes in the HAADF-STEM images are due to K-layers alternating with the $[V_6Sb_6]$ layers. The K atomic columns appear as low-contrast dots between the $[V_6Sb_6]$ layers (Figure 4c). Additionally, we observed a "waving" of K layers, i.e., variation in layer thickness (highlighted with a yellow box in Figure 4a). We attribute this to the denser K-ion packing within certain K-monolayers. This minor variability of K^+ filling within the monolayer is consistent with our synthesis optimization of the KV_6Sb_6 phase, where an excess of KH is required to achieve better crystallinity and to suppress the splitting of certain diffraction peaks emerging from incomplete K filling.[39] A similar phenomenon was observed in the case of layered Li−Ni−B compounds.[64]

For the deintercalated product $K_{0.1(1)}V_6Sb_6$ (Figure 5), the dark stripes corresponding to the K^+ layers become less abundant due to the deintercalation of K^+ (Figure 5a). Deintercalation is further confirmed by the HAADF-STEM intensity profile and EDX analysis (Figures 5b and S9). Upon K^+ deintercalation, the distance between the adjacent $[V_6Sb_6]$ layers decreases from ∼4.2 to ∼3.2 Å (i.e., shrinking of the unit cell along the c-direction), rationalizing the shift of diffraction peaks to higher Q for the $K_{0.1(1)}V_6Sb_6$ phase in the PXRD pattern (Figure 1, diffraction peaks highlighted in yellow).

A close-up analysis of the HAADF-STEM images revealed a difference in the relative shift between the adjacent $[V_6Sb_6]$

https://doi.org/10.1021/jacs.4c07285
J. Am. Chem. Soc. 2024, 146, 26786−26800

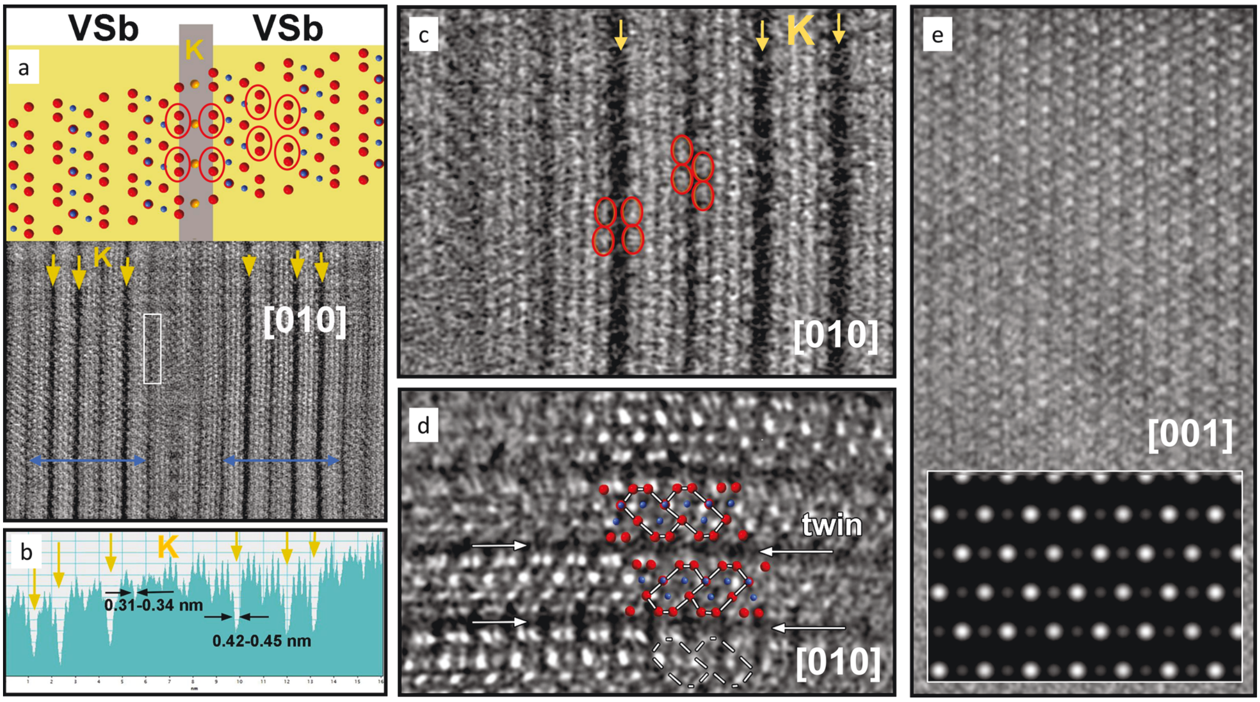

Figure 5. HAADF-STEM data for the $K_{0.1(1)}V_6Sb_6$ phase. (a) [010] HAADF-STEM image indicating the preservation of the $[V_6Sb_6]$ layers upon K^+ deintercalation. The white box highlights the absence of K^+ between the $[V_6Sb_6]$ layers and blue arrows indicate the domain size. (b) HAADF-STEM intensity scan line profile confirming the removal of K^+ and shortening of the interlayer distance between the adjacent $[V_6Sb_6]$ layers upon deintercalation. (c) Magnified [010] HAADF-STEM image revealing the relative shift between the adjacent $[V_6Sb_6]$ layers upon deintercalation. (d) HAADF-STEM image highlighting the different orientation of adjacent $[V_6Sb_6]$ related by C_2 rotation along the *c*-axis. (e) [001] HAADF-STEM image showing a hexagonal symmetry of layers is preserved in the [001] direction; the inset includes the simulated image using the $C2/m$ model. The red ovals in parts (a) and (c) mark the terminating Sb atoms from the adjacent $[V_6Sb_6]$ layers to highlight the relative shift between the layers brought about by deintercalation.

layers across the stacking direction in the absence of K layers between them (Figure 5c, red ovals). When the K^+ layer separates $[V_6Sb_6]$ layers, the terminating Sb atoms from the two adjacent layers are aligned (red ovals to the left in Figure 5c), as also seen for the HAADF-STEM images of the parent KV_6Sb_6 phase (Figure 4a,c,d). However, in the absence of interlayer K^+ ions, there is a relative "sliding" of $[V_6Sb_6]$ layers with respect to each other (red ovals to the right in Figure 5c). Additionally, the STEM images for $K_{0.1(1)}V_6Sb_6$ uncovered one more feature, not seen for the parent KV_6Sb_6 phase: in certain crystallites, a different orientation of adjacent $[V_6Sb_6]$ layers is sporadically seen in selected areas of the sample. These adjacent $[V_6Sb_6]$ layers are related by C_2 rotation along the *c*-axis (180° rotation) (Figure 5d). None of these features were accounted for by the initial models used for structural refinement. Based on the inputs from STEM analysis, we embarked on constructing new models using the scheme shown in Figure 6 to account for the structural features seen in HAADF-STEM images of $K_{0.1(1)}V_6Sb_6$.

The general workflow on how various structural models were built for the deintercalated $K_{0.1(1)}V_6Sb_6$ phase is briefly discussed here and more extensively in the Supporting Information (Figure S10 and Table S1). For each model, the structure was optimized by DFT using vdW relaxation, and their energies are also included for comparison. We started with the $R\bar{3}m$ model of the parent KV_6Sb_6 structure and removed K^+ layers (MODEL 1, Figure 6a). In this model, the adjacent $[V_6Sb_6]$ layers are shifted according to *R*-centering and do not produce a desired relative shift (green rectangle in Figure 6a). In the next step, *R*-centering was removed, resulting in a model with three identical layers (MODEL 2). To model the relative shift between the layers, each layer was shifted relative to the previous layer by (1/6, 1/6, and 0), and the number of layers was extended to six to account for the periodicity of the structure (MODEL 3). Alternatively, to model the relative shift between the layers starting with just two $[V_6Sb_6]$ layers with no relative shift, the α-angle was changed from 90° to ∼105° (MODEL 5) or one layer was shifted by (1/6; 1/6; 0) with respect to other (MODEL 6). Finally, to account for 180° rotation (C_2 rotation along the stacking direction) between the adjacent $[V_6Sb_6]$ layers, as seen in HAADF-STEM images (Figure 5d), MODEL 4 and MODEL 7 were constructed. In MODEL 4, the top three layers were rotated by 180° around the C_2 axis with respect to the bottom three layers while maintaining the (1/6, 1/6, 0) relative shift. In MODEL 7, the same 180° rotation was performed for the top layer, shifted by (1/6, 1/6, 0) with respect to the bottom layer.

The DFT-optimized MODELS 1−7 were used for the refinement of the experimental X-ray PDF data for the $K_{0.1(1)}V_6Sb_6$ phase, and the refinement using MODEL 5 produced the plausible fit of the PDF data, finally uncovering the crystal structure of the $K_{0.1(1)}V_6Sb_6$ phase (Figure 7). It should be noted that DFT optimization with vdW relaxation proved to be a crucial step, providing structural models with low energies, optimized bonding, and reduced interlayer spacing between the adjacent $[V_6Sb_6]$ layers. Table S1 summarizes the unit cell parameters, space group, and DFT-calculated energies of all seven relaxed models. The models without DFT optimization did not yield a good fit to the

https://doi.org/10.1021/jacs.4c07285
J. Am. Chem. Soc. 2024, 146, 26786−26800

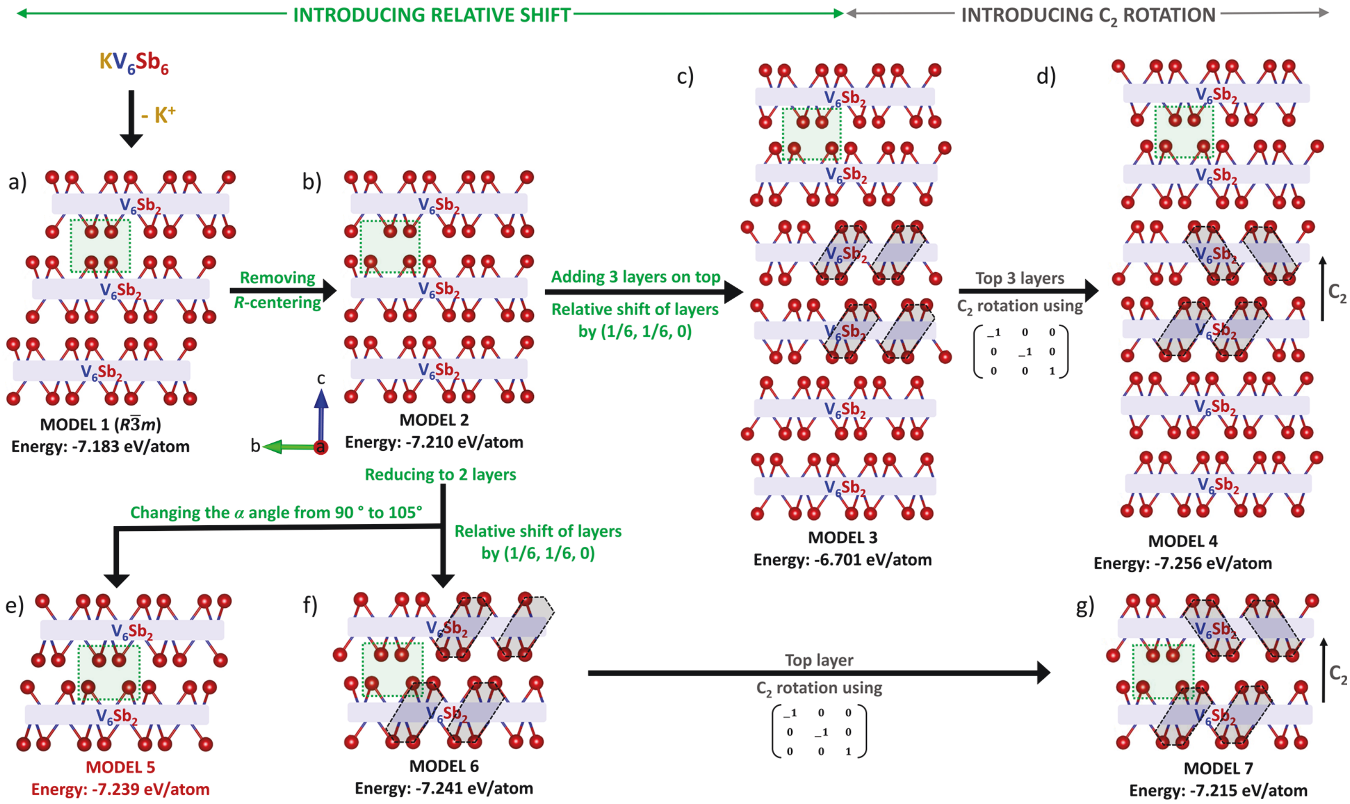

Figure 6. (a−g) Schematic representing the workflow to construct various structural models (MODELS 1−7) for the $K_{0.1(1)}V_6Sb_6$ phase based on the insights from PDF analysis and STEM data. Green rectangles highlight the relative shift (or an absence of it), while the gray regions indicate different orientations of the $[V_6Sb_6]$ layers related by C_2 rotation around the axis shown with a black arrow in panels (d,g). The DFT-calculated energies (eV/atom) obtained from vdW relaxation are included for each model.

experimental PDF data even in the short range (r = 2−11 Å) and resulted in considerable discrepancies between the calculated and experimental PXRD patterns. While DFT optimization was important, the selection of models solely based on DFT-calculated energies without experimental input, such as PDF data refinement, is not viable either. The models have similar energies (Figure 6, Table S1), and MODEL 5 that resulted in the best fit of PDF data is not the one with the lowest energy.

Based on the refinement of PDF data using MODEL 5, the $K_{0.1(1)}V_6Sb_6$ crystallizes in the triclinic space group $P\bar{1}$ (a = 5.52(1) Å, b = 5.54(2) Å, c = 10.24(2) Å, α = 83.6(2)°, β = 83.0(3)°, γ = 59.6(2)°, Z = 2). Analysis of the $P\bar{1}$ model with Platon[63] to check for higher symmetry suggested the monoclinic $C2/m$ model (a = 9.57(2) Å, b = 5.502(8) Å, c = 10.23(2) Å, β = 97.6(2)°, Z = 2). This model is similar to the $C2/m$ model for the parent KV_6Sb_6 phase, except for the absence of K atoms and distinctly larger β angle in KV_6Sb_6 (105.96° in KV_6Sb_6 *v.s.* 97.6(2)° in $K_{0.1(1)}V_6Sb_6$). The $C2/m$ model of $K_{0.1(1)}V_6Sb_6$ accounts for the relative shift between the adjacent $[V_6Sb_6]$ layers (highlighted in the green box in Figure 7a) and shows a clear decrease in the interlayer distance between the $[V_6Sb_6]$ layers to 3.2 Å upon K^+ deintercalation, in excellent agreement with the interlayer distance obtained from STEM analysis. The model works well for the fitting of the experimental PDF data over the r = 2−22 Å range (Figure 7b), equivalent to two unit cells, and also provides a good match to the experimental PXRD data (Figure S11). Since ICP-MS confirms nearly complete K^+ deintercalation from the layered structure, the remaining K^+ can be thought of as nonuniformly dispersed between the $[V_6Sb_6]$ layers, as also seen in the HAADF images (Figure 5a,c). Figure S12a compares the lower symmetry $P\bar{1}$ and the higher symmetry $C2/m$ models for the $K_{0.1(1)}V_6Sb_6$ phase. The lack of certain symmetry constraints for the $P\bar{1}$ space group in comparison to the $C2/m$ space group allows for greater variability in the modeling of the V−V, V−Sb, and Sb−Sb bonding environments, not permitted for the higher symmetry monoclinic model. However, the modeled bond distances for the $P\bar{1}$ model do not significantly differ from the range of distances already accounted for in the $C2/m$ model (Figure S12a). This is reflected in the refinement of the experimental X-ray PDF data, where comparable fitting is observed for the two models (Figure S12b). Please note that a slightly better fitting of the PDF data with the $P\bar{1}$ model is expected, as a greater number of parameters are permitted to be refined.

To further improve the PDF fitting, we refined the anisotropic ADPs (atomic displacement parameters) U_{11}, U_{22}, and U_{33} using the following conditions: $U_{11} = U_{22}$ and $U_{33} = n*U_{11}$, where U_{11} and U_{22} are used to account for the in-plane atomic displacement (within the $[V_6Sb_6]$ layer) and U_{33} accounts for the out-of-plane displacement (across the stacking direction).[65] As seen in Figure S12b, the refinement of anisotropic ADPs using the above constraints further improves the fitting of the PDF data, and for the $C2/m$ model, provides a value of n = 1.8 (n = 2.0 for the $P\bar{1}$ model). A greater value of U_{33} compared to U_{11} and U_{22} is indicative of weaker interatomic correlations between atoms in the stacking direction compared to those within the $[V_6Sb_6]$ layers. The modeling software compensates for these weak out-of-plane

https://doi.org/10.1021/jacs.4c07285
J. Am. Chem. Soc. 2024, 146, 26786−26800

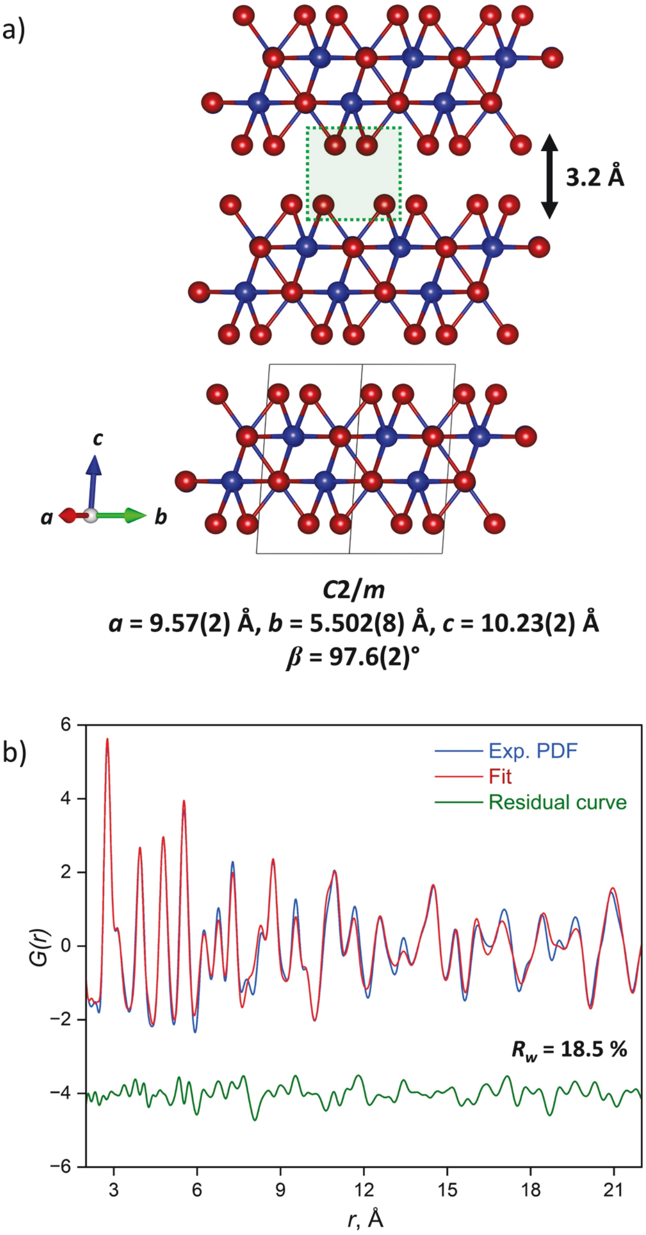

Figure 7. (a) Monoclinic ($C2/m$) crystal structure of $K_{0.1(1)}V_6Sb_6$ revealed via the PDF-STEM-DFT synergistic approach and (b) fitting of the X-ray PDF data in the r = 2−22 Å range using the $C2/m$ model resulting in a good fit.

interatomic correlations with an enlarged ADP in the stacking direction. The enlarged ADP is most likely indicative of stacking faults, as the [V_6Sb_6] layers stack along the c-axis. A similar phenomenon is observed in other materials, such as layered graphite and CdSe nanoparticles.[66,67] Based on the above discussion, the greater variability in modeling of the structural parameters afforded by the lower symmetry $P\overline{1}$ space group can be considered minor features of the local structure but not a feature of the structure at large. Therefore, we propose the $C2/m$ crystal structure to be a plausible model for the $K_{0.1(1)}V_6Sb_6$ phase. Table S2 lists the atomic coordinates, site multiplicity, anisotropic atomic displacement parameters, and occupancy of all of the atomic sites in the $C2/m$ structure of $K_{0.1(1)}V_6Sb_6$.

Based on the PDF data refinement, a domain size of ∼50 Å can be estimated for the deintercalated phase, which is further supported by STEM, where periodicity is observed over five [V_6Sb_6] layers, each ∼10 Å wide (blue arrows in Figure 5a). Domain size estimation from PXRD data is unreliable because of the uneven broadness of the diffraction peaks; however, a good fitting of the experimental PXRD supports the plausibility of the determined $C2/m$ crystal structure for the deintercalated phase (Figure S11).

Other models were also used for the refinement of the experimental PDF data for $K_{0.1(1)}V_6Sb_6$. A r-dependent fitting up to r = 27 Å (Figure S13), as well as fitting in the short (r = 2−9 Å), middle (r = 9−18 Å), and long (r = 18−27 Å) ranges (Figure S14), was performed using MODELS 3−7. MODELS 3, 4, 6, and 7 contain a significantly higher number of atoms and/or have a lower symmetry compared to the $C2/m$ model (MODEL 5); therefore, more parameters could be refined. However, the resulting structural models display unreasonably short V−Sb bond distances of 2−2.3 Å. Such short distances are not observed for refinements with MODEL 5 ($C2/m$ model). MODEL 5 for the $K_{0.1(1)}V_6Sb_6$ phase provides the best fit in the r = 2−27 Å range, as well as for fitting in the short, middle, and long ranges, confirming its plausibility. Refer to Figures S13 and S14 for further details. Note that the $C2/m$ model does not account for a trace amount of residual K^+ and the sporadically observed different orientations of [V_6Sb_6] layers (Figure 5d). We hypothesize that layer-by-layer K^+ deintercalation could result in crystallites with certain faults. Nonetheless, the proposed monoclinic model ($C2/m$) is a good representation of the average structure for the 2D Kagome antimonide $K_{0.1(1)}V_6Sb_6$, leading to a decent fit of the PDF data (Figures 7, S13, and S14).

Figure 8 compares the $C2/m$ crystal structures of the parent KV_6Sb_6 and $K_{0.1(1)}V_6Sb_6$ phases. Consistent with PXRD, PDF, DFT, and STEM data, the [V_6Sb_6] layers in $K_{0.1(1)}V_6Sb_6$ bear close resemblance to those in parent KV_6Sb_6. Careful analysis reveals the variation in the V−Sb, V−V, and Sb−Sb bond distances, which is a direct consequence of the change in unit cell parameters upon deintercalation (Figure 8b). The bonding environments for V and Sb atoms are maintained (Figure 8b) but with small variations in the bond distances, as indicated in Figure 8b. The pairwise correlations (V−V, Sb−Sb, and V−Sb) calculated for the $C2/m$ model of KV_6Sb_6 and $K_{0.1(1)}V_6Sb_6$ are comparable, supporting our claim of similar bond distances for the two (Figure S15). The V-Kagome network in KV_6Sb_6 remains corrugated upon deintercalation with a V−V distance in the 2.71−2.91 Å range. The terminating Sb atoms from the [V_6Sb_6] layer in $K_{0.1(1)}V_6Sb_6$ form a hexagonal network with the Sb−Sb distances of 3.17 and 3.21 Å, as compared to the Sb−Sb distances of 3.13 and 3.29 Å in KV_6Sb_6.

While the interlayer distance between [V_6Sb_6] layers in $K_{0.1(1)}V_6Sb_6$ is 3.2 Å, the shortest distance between terminating Sb atoms from the adjacent [V_6Sb_6] layers is 3.5 Å, suggestive of vdW interaction (Figure 8). In inorganic solids, a Sb−Sb distance of 2.8−3.2 Å is expected for Sb−Sb covalent bonding.[68,69] For example, a Sb−Sb distance of ∼3.1 Å is seen between Sb atoms forming a flat square net in the layered REGaSb_2 (RE = La−Nd, Sm) compounds.[68] Another example is provided by the $RE_{14}MSb_{11}$ (RE = Yb, Eu, M = Mn, Zn, Cd) family, where Sb atoms form a linear Sb_3^{7-} anionic unit with a Sb−Sb distance of ∼3.2 Å.[69] Thus, we estimate the upper limit of covalent Sb−Sb bonding as 3.2 Å. The vdW radius for the Sb atom is ∼2.0 Å,[70,71] and hence, an expected Sb−Sb distance

https://doi.org/10.1021/jacs.4c07285
J. Am. Chem. Soc. 2024, 146, 26786−26800

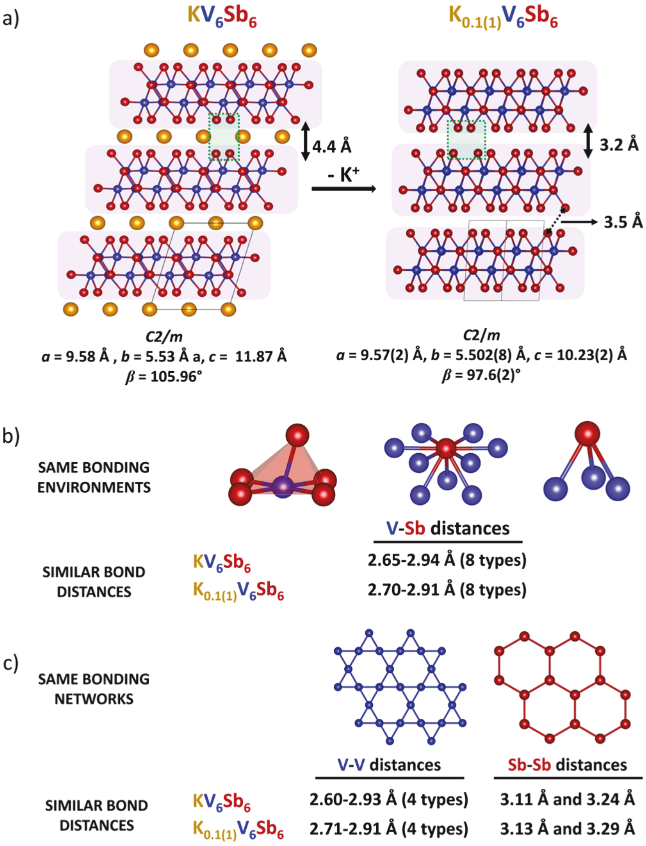

Figure 8. Comparison of (a) $C2/m$ crystal structure of the parent KV_6Sb_6 compound and its deintercalated derivative $K_{0.1(1)}V_6Sb_6$, (b) coordination environments for V and Sb atoms, and (c) networks for V and Sb atoms, indicating minor changes in V−Sb, V−V, and Sb−Sb distances or bonding environment upon deintercalation.

for vdW interaction is 4.0 Å. In $K_{0.1(1)}V_6Sb_6$, the shortest Sb−Sb distance of 3.5 Å between the adjacent $[V_6Sb_6]$ layers falls in the range of 3.2−4.0 Å, suggestive of comparatively strong vdW interactions between the adjacent $[V_6Sb_6]$ layers. In fact, the Sb−Sb distance in $K_{0.1(1)}V_6Sb_6$ is longer than the Sb−Sb distance of 3.3 Å in the naturally occurring vdW material—elemental Sb, where each Sb atom has 3 + 3 coordination consisting of three short 2.9 Å distances (covalent bonds) and three longer 3.3 Å contacts (vdW interaction).[72] Therefore, the new $K_{0.1(1)}V_6Sb_6$ compound obtained via K^+ deintercalation is a 2D material with a vdW gap of 3.2 Å.

Overall, the structure of $K_{0.1(1)}V_6Sb_6$ produced via deintercalation of K^+ from KV_6Sb_6 closely resembles the parent phase, yet nearly complete deintercalation of K^+ results in the relative shift between the adjacent $[V_6Sb_6]$ layers, not seen for the parent phase. As a result, the 2D metastable vanadium antimonide with a vdW gap of 3.2 Å arising from the weakly bonded Sb atoms from the adjacent $[V_6Sb_6]$ layers is obtained. Deintercalation of K^+ only slightly alters the bond distances and coordination environments within the $[V_6Sb_6]$ layers, proving the substantial flexibility of the layered structure.

Calculation of the Electronic Structure and T_c of $K_{0.1(1)}V_6Sb_6$. As mentioned earlier, the parent KV_6Sb_6 compound features a Kagome bilayer of V atoms.[39−41] The Kagome lattice consisting of moment-bearing atoms oftentimes introduces magnetic frustration, yielding intriguing electronic and magnetic properties.[23−27,31] DFT electronic structure calculations for the KV_6Sb_6 compound reveal Dirac Fermion behavior.[40,42] Additionally, band crossing close to the Fermi level discloses a nontrivial band topology, desirable for quantum spin liquid and superconductivity.[27,40] In fact, KV_6Sb_6 displays pressure-induced superconductivity with a $T_{c,max}$ of 0.37 K at 31 GPa.[41] Considering the retention of the V-Kagome net in $K_{0.1(1)}V_6Sb_6$, we calculated the electronic and phonon band structure for $K_{0.1(1)}V_6Sb_6$.

DFT calculations of the electronic band structure and density of states (DOS) were performed for the K-free $C2/m$ structural model of $K_{0.1(1)}V_6Sb_6$, using the experimentally obtained, room-temperature unit cell parameters (Figure 9).

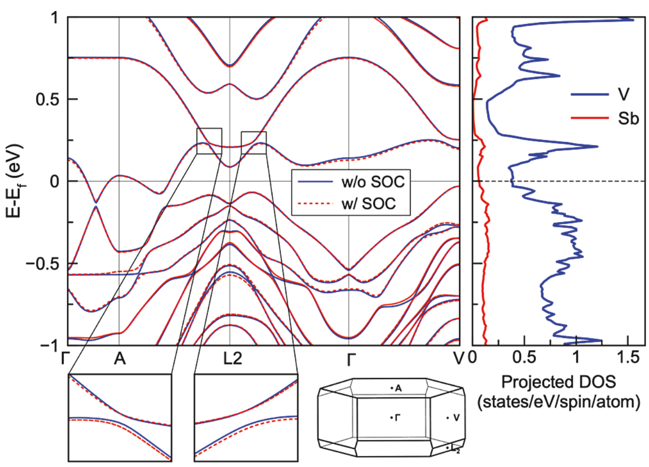

Figure 9. DFT-calculated electronic band structure and DOS diagram for the experimental $C2/m$ model of the $K_{0.1(1)}V_6Sb_6$ compound. The inset panels show zoomed-in parts of the band structure to highlight the opening of the band crossing along A-L2-Γ, not seen in the band structure of KV_6Sb_6.

The Dirac band crossing identified in KV_6Sb_6[40,42] opens up in the $K_{0.1(1)}V_6Sb_6$ structure (inset in Figure 9). The spin−orbit coupling has little effect on the calculated band structure. The change in the band topology upon deintercalation can be attributed to the local symmetry breaking in the $K_{0.1(1)}V_6Sb_6$ structure. A comparison of the band structures for KV_6Sb_6 and $K_{0.1(1)}V_6Sb_6$ reveals flatter bands along the L2-Γ-V for $K_{0.1(1)}V_6Sb_6$, suggesting more localized electrons in the $[V_6Sb_6]$ layers as a result of deintercalation. A nonzero DOS at the Fermi level (E_f) suggests metallic behavior for the $K_{0.1(1)}V_6Sb_6$ compound with considerable contribution from V-3d atomic orbitals compared to the Sb-5p orbitals, both above and below the E_f (Figure 9). The calculated phonon band structure for the experimental $C2/m$ model of $K_{0.1(1)}V_6Sb_6$ has imaginary modes, indicative of an increased dynamic instability upon deintercalation and consistent with the metastability of $K_{0.1(1)}V_6Sb_6$ (Figure S16).

To perform the electron-phonon coupling (EPC) calculations while maintaining the layered structure, the $C2/m$ structure was transformed into the lower symmetry $P\bar{1}$ model and fully relaxed. The relaxation leads to a shorter Sb−Sb interlayer distance of 2.7 Å and a slightly lower energy (−7.28 eV/atom for the relaxed model vs −7.16 eV/atom for the experimental model), while a minor variation in the calculated band structure (Figures S17a,b) is observed. The EPC calculations performed on the $P\bar{1}$ relaxed model suggest a decent degree of EPC, with a coupling constant, λ = 0.42, comparable to $\lambda \sim 0.60$ for the superconductor MgB_2 (Figure

https://doi.org/10.1021/jacs.4c07285
J. Am. Chem. Soc. 2024, 146, 26786−26800

S17c). A comparable value of λ indicates the possibility of a superconducting transition. However, extremely low phonon frequencies imply a T_c close to 0 K (0.47 K). The EPC remains unchanged with the inclusion of the vdW correction (Figure S17d). Overall, electronic structure calculations performed for the K-free structural models of $K_{0.1(1)}V_6Sb_6$ suggest the variation in the band structure due to deintercalation, while the topological band structure features inherited from the KV_6Sb_6 parent are preserved.

Magnetic and Transport Properties of $K_{0.1(1)}V_6Sb_6$. (De)intercalation of atoms/ions in a layered material often leads to alteration of its electronic structure and, thus, physical properties.[11] Previously,[39] we characterized the magnetic and transport properties of the parent KV_6Sb_6 phase and will use it and another ternary compound, KV_3Sb_5,[38] with a Kagome monolayer of V atoms for a direct comparison with the deintercalated $K_{0.1(1)}V_6Sb_6$ phase (Figure S18).

Figure 10a shows the temperature dependence of molar susceptibility (χ) for $K_{0.1(1)}V_6Sb_6$ measured at a 0.1 T applied magnetic field. Magnetic susceptibility of the $K_{0.1(1)}V_6Sb_6$ phase ($\chi \sim 5 \times 10^{-4}$ emu/mol per V atom in the 100−300 K range) is comparable to that of the parent KV_6Sb_6 phase ($\chi = 6.0 \times 10^{-4}$ emu/mol per V atom in the 20−300 K range).[39] Neither a splitting of the zero-field cooled (ZFC) and field cooled (FC) curves nor a superconducting transition is observed for the deintercalated phase down to 2 K, as confirmed by ac susceptibility measurement.

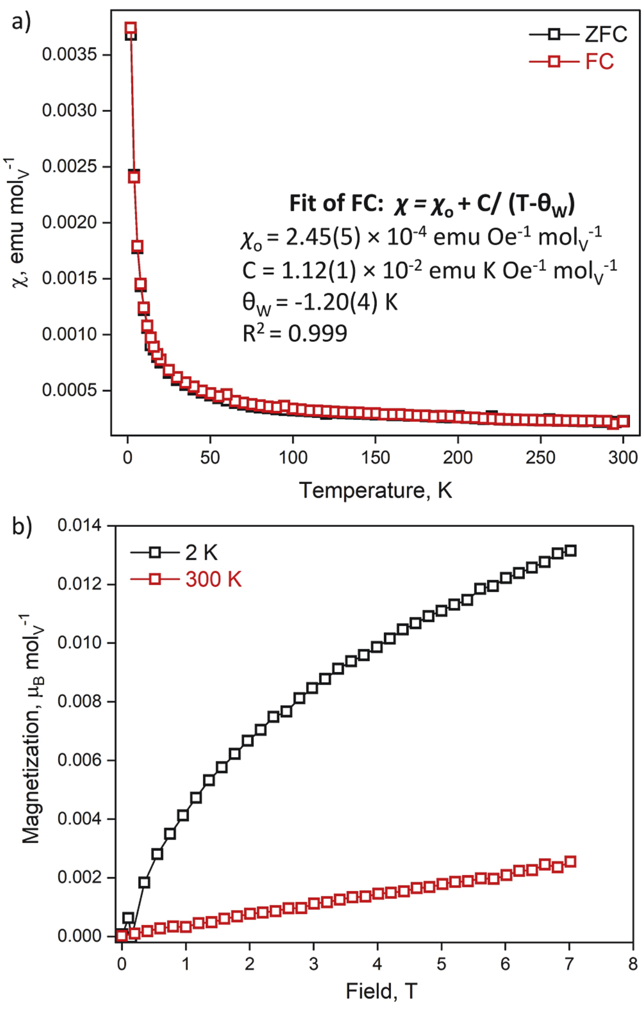

Figure 10. Magnetic properties for the deintercalated $K_{0.1(1)}V_6Sb_6$ phase: (a) ZFC-FC temperature dependence of molar susceptibility (χ) obtained at a 0.1 T applied magnetic field in the 2−300 K temperature range and (b) field dependence of magnetization at 2 and 300 K.

The fitting of the FC curve for $K_{0.1(1)}V_6Sb_6$ using the modified Curie−Weiss law ($\chi = \chi_0 + C/[T - \theta_w]$, where χ_0 is the temperature independent term, C is the Curie constant, and θ_w is the Weiss temperature) results in a low value of θ_w = −1.2 K and a low effective moment per V atom (μ_{eff} per V atom = 0.30 μ_B), consistent with a nearly temperature-independent paramagnetism in $K_{0.1(1)}V_6Sb_6$. The Curie−Weiss parameters for ternary phases KV_6Sb_6 and KV_3Sb_5 are similar to those obtained for $K_{0.1(1)}V_6Sb_6$ (Figure S18). The paramagnetism in $K_{0.1(1)}V_6Sb_6$ is further supported by a linear dependence of magnetization on the field at 300 K (Figure 10b). A deviation from linearity at 2 K is a result of weakly interacting moments with an applied magnetic field at temperatures near absolute zero.

In conclusion, $K_{0.1(1)}V_6Sb_6$ is a Curie−Weiss paramagnet with a strong temperature-independent contribution and low effective moment per V atom, displaying similar temperature and field-dependent magnetic properties as the parent KV_6Sb_6 and structurally related KV_3Sb_5 compounds. Essentially, the deintercalation of K^+ does not affect the magnetic behavior to a great extent.

We also investigated the low-temperature transport properties of the $K_{0.1(1)}V_6Sb_6$ phase to determine its potential for thermoelectric applications. Thermoelectric materials convert heat into electricity and vice versa and are characterized by a unitless figure of merit $zT = S^2T/\rho\kappa$, where T is the temperature, ρ is the electrical resistivity, S is the Seebeck coefficient, and κ is the thermal conductivity. For efficient thermoelectric materials, high zT values could be achieved via optimizing carrier concentrations to tune the electrical and thermal transport properties. Narrow-band semiconductors with complex structures and/or heavy atoms are the best candidates for thermoelectric applications, and there is a handful of thermoelectric antimonides reported.[73,74]

Measurements of electrical resistivity (ρ), Seebeck Coefficient (S), and thermal conductivity (κ) were performed on a cold-pressed pellet of $K_{0.1(1)}V_6Sb_6$ with ~75% compactness in the 5−300 K temperature range (Figure 11). Attempts were made at sintering powders using SPS; however, decomposition to form Sb was observed at temperatures as low as 473 K, consistent with high-temperature in situ studies (Figure 2). While the magnetic properties of the deintercalated and the parent phases are similar, the transport properties of the two are distinct. Resistivity (ρ) decreases almost linearly with an increase in temperature, revealing a heavily doped semiconductor behavior for $K_{0.1(1)}V_6Sb_6$, different from the metallic behavior observed in KV_6Sb_6.[39] The resistivity at 300 K is ~210 mΩ cm, which is 2 orders of magnitude higher compared to the resistivity of KV_6Sb_6 (ρ = 1.65 mΩ cm at 300 K).[39] DFT calculations show a nonzero DOS at E_f (Figure 9) and the Tauc plot obtained from the measurement of diffused reflectance of the $K_{0.1(1)}V_6Sb_6$ phase (Figure S19) shows no band gap down to 0.5 eV, both suggesting a metallic/heavily doped semiconductor behavior for $K_{0.1(1)}V_6Sb_6$.

The metallic nature of the $K_{0.1(1)}V_6Sb_6$ compound is further supported by a low value of the Seebeck coefficient ($S = -3$ μV K^{-1} at 300 K). Both $K_{0.1(1)}V_6Sb_6$ and KV_6Sb_6 ($S = 8$ μV K^{-1} at 300 K)[39] have a low value of Seebeck coefficient, but

https://doi.org/10.1021/jacs.4c07285
J. Am. Chem. Soc. 2024, 146, 26786−26800

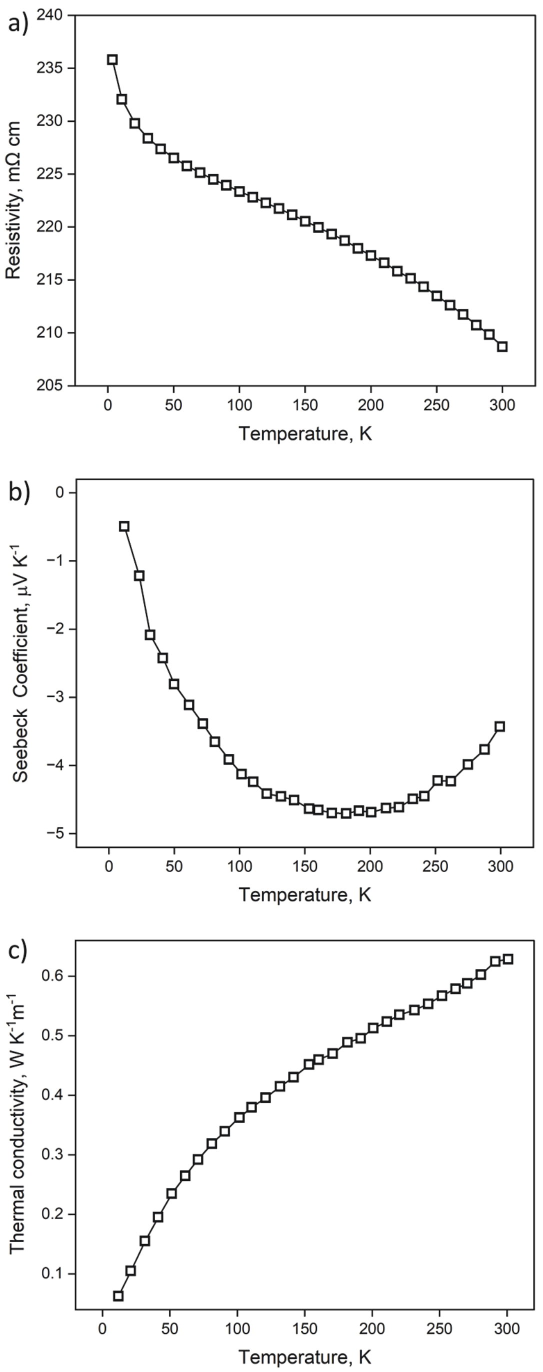

Figure 11. Measurement of low-temperature transport properties of the $K_{0.1(1)}V_6Sb_6$ phase: (a) resistivity (ρ), (b) Seebeck coefficient (S), and (c) thermal conductivity (κ). Measurements were performed on a pellet with 75% density.

deintercalation changes the type of charge carrier from holes in KV_6Sb_6 to electrons in $K_{0.1(1)}V_6Sb_6$. The thermal conductivity κ_{total} and its temperature dependence are similar for the two antimonides: 0.6 W K^{-1} m^{-1} for $K_{0.1(1)}V_6Sb_6$ *v.s.* 1.0 W K^{-1} m^{-1} for KV_6Sb_6 at 300 K.[39] Lattice thermal conductivity ($\kappa_{lattice}$) accounts for 99% of the total thermal conductivity, indicating very low electronic contribution (κ_{el}) for $K_{0.1(1)}V_6Sb_6$. An overall low thermal conductivity is desirable for thermoelectric applications, yet we ought to mention that the transport properties of $K_{0.1(1)}V_6Sb_6$ were measured on a cold-pressed sample with a moderate compactness of 75%, hindering the evaluation of intrinsic properties of $K_{0.1(1)}V_6Sb_6$.

With a low value of thermal conductivity, structural and compositional tuning to optimize ρ and S can be performed to enhance the thermoelectric properties of the material. However, given the metastable nature of the $K_{0.1(1)}V_6Sb_6$ phase, an alternative way would be to first perform doping of the parent KV_6Sb_6 phase, followed by deintercalation of K^+ to access doped variants of the $[V_6Sb_6]$ layers. The ease of K^+ deintercalation from KV_6Sb_6 resulting in $K_{0.1(1)}V_6Sb_6$ suggests that the $[V_6Sb_6]$ layered structure might be amenable for doping, offering a flexible platform for new 2D materials. Motivated by this, we attempted ion exchange in KV_6Sb_6.

Proof-of-Concept Ion-Exchange Studies on KV_6Sb_6. The KV_6Sb_6 compound containing alternating layers of K^+ and $[V_6Sb_6]^-$ is an attractive candidate for ion-exchange studies. Encouraged by examples of successful exchange of Sr^{2+} for K^+ in the layered sulfide $K_{2x}Mn_xSn_{3-x}S_6$ (KMS-1) by Manos et al.,[46] we explored ion exchange in the KV_6Sb_6 compound using solvothermal and nonsolvothermal routes. The obtained data show that the K^+ ion can be exchanged with Na^+, Rb^+, and Cs^+ (Figures S20−S22, Table S4). The analogs of the KV_6Sb_6 phase are reported for Rb and Cs[40,41] but not for Na, Ca, Sr, or Ba. Similarly, only K, Rb, and Cs analogs have been reported for the AV_3Sb_5 family. While successful ion exchange of K with Rb and Cs would serve as a proof-of-concept, for other ions, ion exchange could provide a suitable avenue for the synthesis of the AV_6Sb_6 analogs, not accessible via high-temperature routes.

For the nonsolvothermal ion exchange with chloride salts of alkali and alkaline earth metals, PXRD data indicate successful partial ion exchange only with Rb^+ and Cs^+. Deintercalation was instead observed in the case of Na^+, Ca^{2+}, Sr^{2+}, and Ba^{2+} ions (Figure S20). The ion exchange was evaluated using SEM-EDX analysis, the results of which are summarized in Table S4. Decent levels of exchange are observed for RbCl and CsCl (~25−45%); however, a decrease in the overall amount of alkali metals indicates the beginning of deintercalation during the ion exchange process when carried out in water (Table S4, experiments 2 and 3). This suggested a competition between the deintercalation and ion exchange processes in an aqueous medium.

To eliminate this competition, it was necessary to use a nonaqueous solvent, in which the parent KV_6Sb_6 undergoes little, to preferably, no deintercalation. Therefore, we performed the ion exchange in MeOH since a lower rate of K^+ deintercalation was observed in MeOH compared to that in water (Figure S1). To make up for the poor solubility of chloride salts in MeOH compared to water (RbCl = 1.07 g/100 mL and CsCl = 2.59 g/100 mL at 298 K),[75] we resorted to the solvothermal route for ion exchange. Solvothermal synthesis allows for exchange reactions at elevated temperatures and pressures, which improves the dissolution of a salt in a given solvent. Using MeOH successfully eliminated deintercalation; however, the extent of exchange with RbCl under solvothermal conditions was lower than that previously observed in water (Table S4, experiments 2 vs 4). When the chlorides were replaced with carbonates, Rb_2CO_3 and Cs_2CO_3, an increased rate of exchange was achieved (Table S4, experiments 4 vs 5 and 11) due to the significantly improved solubility of the carbonate salts in MeOH (Rb_2CO_3 = 19.76 g/100 mL and Cs_2CO_3 = 44.52 g/100 mL at 298 K). With enhanced ion exchange under solvothermal conditions for the carbonates, the reaction temperature and time were varied in an effort to further maximize the ion exchange for Rb^+ and Cs^+, details of which are included in the SI (Figures S21 and S22, Table S4, experiments 4−12). The highest exchange rate of K^+ at around 50% was achieved at 423 K for 2 h for both Rb^+ and Cs^+ (Table S4, experiments 7 and 12).

Encouraged by the success of the solvothermal route for ion exchange in KV_6Sb_6, we attempted Na^+ exchange in MeOH using CH_3COONa. During our exploration of new phases in the K−V−Sb system using the hydride route,[39] we also explored the Na−V−Sb and Na−K−V-Sb systems. Both ex situ and in situ experiments suggested the presence of a structurally related "NaV_6Sb_6" phase, albeit these efforts remained inconclusive. SEM-EDX analysis of solvothermal reactions of KV_6Sb_6 with CH_3COONa indicates that ∼17% K^+ can be exchanged with Na^+ (Table S4, experiment 13), providing the first example of a compound with Na^+ cations introduced between [V−Sb] layers. The Na exchange is nonuniform, and the extent of ion exchange is lower compared to those of Rb^+ and Cs^+. Refer to Figure S23 for more information on Na exchange.

The above results clearly demonstrate that the ion exchange can be successfully achieved in the layered KV_6Sb_6 phase, further showcasing its flexibility for structural manipulation. Alternative routes, such as electrochemical ion exchange, can be used to improve the efficiency of the process and hold promise in obtaining structurally related materials, especially metastable phases, which cannot be synthesized via high-temperature routes.

■ CONCLUSIONS

A new metastable 2D-Kagome pnictide $K_{0.1(1)}V_6Sb_6$ was synthesized via a "soft chemical" route, involving facile deintercalation of K^+ from the layered KV_6Sb_6 compound using water. Deintercalation is irreversible and quantitatively determined by using ICP-MS and SEM-EDX. PXRD, PDF, and STEM analyses confirm the preservation of the $[V_6Sb_6]$ layers upon deintercalation, separated by a vdW gap of 3.2 Å. The structure of the $K_{0.1(1)}V_6Sb_6$ phase was determined by using the complementary PDF-STEM-DFT techniques, highlighting the importance of utilizing synergistic methods for the bulk structural determination of metastable 2D materials. The $K_{0.1(1)}V_6Sb_6$ phase crystallizes in the $C2/m$ space group similar to the parent KV_6Sb_6 phase, albeit with a relative shift of the $[V_6Sb_6]$ layers in $K_{0.1(1)}V_6Sb_6$. The magnetic properties of the parent and deintercalated phases are comparable, both displaying nearly temperature-independent paramagnetism. Calculation of the electronic band structure reveals the nontrivial band topology with flat bands and opening of band crossing afforded by deintercalation. Measurement of transport properties reveals a low thermal conductivity of 0.6 $W\ K^{-1}\ m^{-1}$ for $K_{0.1(1)}V_6Sb_6$, similar to parent KV_6Sb_6. The overall low electrical resistivity and thermopower of $K_{0.1(1)}V_6Sb_6$ suggest metallic/heavily doped semiconductor behavior. Additionally, we show that the layered antimonide KV_6Sb_6 is prone to ion exchange via a solvothermal route and confirm the inclusion of Na^+ between the [V−Sb] layers, which is unattainable via high-temperature routes.

The methodologies discussed in this work can be extended to other layered pnictides in search of new pnictide-based 2D materials that are barely studied compared to their 2D chalcogenide counterparts. The demonstrated flexibility of the KV_6Sb_6 layered structure opens up new avenues for structural manipulation via doping or electrochemical ion exchange, providing a rich playground to access new 2D materials with emergent properties.

■ ASSOCIATED CONTENT

Supporting Information

The Supporting Information is available free of charge at https://pubs.acs.org/doi/10.1021/jacs.4c07285.

Additional PXRD data, SEM images, PDF refinement plots, TEM-EDX data, tables with crystallographic data, Rietveld refinement plot, DFT-calculated electronic and phonon band structures and DOS diagrams, magnetic property plots, and data for ion-exchange studies (PDF)

Accession Codes

CCDC 2356990 contains the supplementary crystallographic data for this paper. These data can be obtained free of charge via www.ccdc.cam.ac.uk/data_request/cif, or by emailing data_request@ccdc.cam.ac.uk, or by contacting The Cambridge Crystallographic Data Centre, 12 Union Road, Cambridge CB2 1EZ, U.K.; fax: +44 1223 336033.

■ AUTHOR INFORMATION

Corresponding Author

Julia V. Zaikina − *Department of Chemistry, Iowa State University, Ames, Iowa 50011, United States;* orcid.org/0000-0002-8755-1926; Email: yzaikina@iastate.edu

Authors

Aishwarya Mantravadi − *Department of Chemistry, Iowa State University, Ames, Iowa 50011, United States*

Bradyn C. Weaver − *Department of Chemistry, Iowa State University, Ames, Iowa 50011, United States*

Shiya Chen − *Department of Physics, Xiamen University, Xiamen 361005, China*

Shahnaz Mukta − *Department of Chemistry, Iowa State University, Ames, Iowa 50011, United States*

Yao Abusa − *Department of Chemistry, Iowa State University, Ames, Iowa 50011, United States;* orcid.org/0000-0003-2508-5330

Arka Sarkar − *Department of Chemistry, Iowa State University, Ames, Iowa 50011, United States; Ames National Laboratory, US Department of Energy, Ames, Iowa 50011, United States;* orcid.org/0000-0002-5996-7537

Yang Sun − *Department of Physics, Xiamen University, Xiamen 361005, China*

Yaroslav Mudryk − *Ames National Laboratory, US Department of Energy, Ames, Iowa 50011, United States;* orcid.org/0000-0003-2658-0413

Alexander Gundlach-Graham − *Department of Chemistry, Iowa State University, Ames, Iowa 50011, United States;* orcid.org/0000-0003-4806-6255

Kai-Ming Ho − *Department of Physics and Astronomy, Iowa State University, Ames, Iowa 50011, United States*

Oleg I. Lebedev − *Laboratoire CRISMAT, ENSICAEN-CNRS, UMR 6508, 14050 Caen, France*

Complete contact information is available at: https://pubs.acs.org/10.1021/jacs.4c07285

Notes

The authors declare no competing financial interest.

https://doi.org/10.1021/jacs.4c07285
J. Am. Chem. Soc. 2024, 146, 26786−26800

■ ACKNOWLEDGMENTS

Financial support from the National Science Foundation (U.S.) Division of Materials Research (DMR-1944551) CAREER Award is gratefully acknowledged. We thank Prof. Karena W. Chapman (Department of Chemistry, Stony Brook University) for the help with the analysis of the total scattering data, Dr. Warren Straszheim (Materials Analysis Research Laboratory, Iowa State University) for the help with SEM-EDX data acquisition, and Prof. Kirill Kovnir (Department of Chemistry, Iowa State University, and DOE Ames Laboratory) for the access to PXRD, DSC and PPMS. Shaorong Fang and Tianfu Wu from the Information and Network Center of Xiamen University are acknowledged for helping with GPU computing. S.M. and A.G.-G. acknowledge Analytik Jena for providing the MICAP-MS instrument used in the study for ICP-MS analysis. Use of the Advanced Photon Source at Argonne National Laboratory (APS ANL) was supported by the U.S. Department of Energy, Office of Science, Office of Basic Energy Sciences, under Contract No. DE-AC02-06CH11357. Dr. W. Xu at 17-BM at APS ANL is acknowledged for the help with high-temperature synchrotron PXRD data collection. The magnetic measurements were supported by the Division of Materials Science and Engineering of the Office of Basic Energy Sciences the Office of Science of the U.S. Department of Energy through the Ames National Laboratory. Ames National Laboratory is operated by Iowa State University for the DOE under Contract No. DE-AC02-07CH11358. The work at Xiamen University was supported by the Natural Science Foundation of Xiamen (grant no. 3502Z202371007), the Fundamental Research Funds for the Central Universities (grant No. 20720230014) and NSFC (grant no. 42374108).

■ REFERENCES

(1) Bhimanapati, G. R.; Lin, Z.; Meunier, V.; Jung, Y.; Cha, J.; Das, S.; Xiao, D.; Son, Y.; Strano, M. S.; Cooper, V. R.; Liang, L.; Louie, S. G.; Ringe, E.; Zhou, W.; Kim, S. S.; Naik, R. R.; Sumpter, B. G.; Terrones, H.; Xia, F.; Wang, Y.; Zhu, J.; Akinwande, D.; Alem, N.; Schuller, J. A.; Schaak, R. E.; Terrones, M.; Robinson, J. A. Recent Advances in Two-Dimensional Materials beyond Graphene. *ACS Nano* **2015**, *9* (12), 11509−11539.

(2) Butler, S. Z.; Hollen, S. M.; Cao, L.; Cui, Y.; Gupta, J. A.; Gutiérrez, H. R.; Heinz, T. F.; Hong, S. S.; Huang, J.; Ismach, A. F.; Johnston-Halperin, E.; Kuno, M.; Plashnitsa, V. V.; Robinson, R. D.; Ruoff, R. S.; Salahuddin, S.; Shan, J.; Shi, L.; Spencer, M. G.; Terrones, M.; Windl, W.; Goldberger, J. E. Progress, Challenges, and Opportunities in Two-Dimensional Materials beyond Graphene. *ACS Nano* **2013**, *7* (4), 2898−2926.

(3) Yankowitz, M.; Chen, S.; Polshyn, H.; Zhang, Y.; Watanabe, K.; Taniguchi, T.; Graf, D.; Young, A. F.; Dean, C. R. Tuning Superconductivity in Twisted Bilayer Graphene. *Science* **2019**, *363* (6431), 1059−1064.

(4) Cao, Y.; Fatemi, V.; Fang, S.; Watanabe, K.; Taniguchi, T.; Kaxiras, E.; Jarillo-Herrero, P. Unconventional Superconductivity in Magic-Angle Graphene Superlattices. *Nature* **2018**, *556* (7699), 43−50.

(5) Manzeli, S.; Ovchinnikov, D.; Pasquier, D.; Yazyev, O. V.; Kis, A. 2D Transition Metal Dichalcogenides. *Nat. Rev. Mater.* **2017**, *2* (8), 1−15.

(6) Thakur, A.; Chandran, B.S. N.; Davidson, K.; Bedford, A.; Fang, H.; Im, Y.; Kanduri, V.; Wyatt, B. C.; Nemani, S. K.; Poliukhova, V.; Kumar, R.; Fakhraai, Z.; Anasori, B. Step-by-Step Guide for Synthesis and Delamination of $Ti_3C_2T_x$ MXene. *Small Methods* **2023**, *7* (8), No. 2300030.

(7) Naguib, M.; Barsoum, M. W.; Gogotsi, Y. Ten Years of Progress in the Synthesis and Development of MXenes. *Adv. Mater.* **2021**, *33* (39), No. 2103393.

(8) Gogotsi, Y.; Anasori, B. The Rise of MXenes. *ACS Nano* **2019**, *13* (18), 8491−8494.

(9) Zhang, B.; Zhou, J.; Sun, Z. MBenes: Progress, Challenges and Future. *J. Mater. Chem. A* **2022**, *10* (30), 15865−15880.

(10) Alameda, L. T.; Moradifar, P.; Metzger, Z. P.; Alem, N.; Schaak, R. E. Topochemical Deintercalation of Al from MoAlB: Stepwise Etching Pathway, Layered Intergrowth Structures, and Two-Dimensional MBene. *J. Am. Chem. Soc.* **2018**, *140* (28), 8833−8840.

(11) Bhaskar, G.; Gvozdetskyi, V.; Batuk, M.; Wiaderek, K. M.; Sun, Y.; Wang, R.; Zhang, C.; Carnahan, S. L.; Wu, X.; Ribeiro, R. A.; Bud'ko, S. L.; Canfield, P. C.; Huang, W.; Rossini, A. J.; Wang, C. Z.; Ho, K. M.; Hadermann, J.; Zaikina, J. V. Topochemical Deintercalation of Li from Layered LiNiB: Toward 2D MBene. *J. Am. Chem. Soc.* **2021**, *143* (11), 4213−4223.

(12) Sasaki, S.; Clarke, S. J.; Jobic, S.; Cario, L. Anionic Redox Topochemistry for Materials Design: Chalcogenides and Beyond. *ACS Org. Inorg. Au.* **2024**, *4* (1), 26−40.

(13) Zhou, X.; Wilfong, B.; Vivanco, H.; Paglione, J.; Brown, C. M.; Rodriguez, E. E. Metastable Layered Cobalt Chalcogenides from Topochemical Deintercalation. *J. Am. Chem. Soc.* **2016**, *138* (50), 16432−16442.

(14) Rodriguez, E. E.; Zavalij, P.; Hsieh, P. Y.; Green, M. A. Iodine as an Oxidant in the Topotactic Deintercalation of Interstitial Iron in $Fe_{1+x}Te$. *J. Am. Chem. Soc.* **2010**, *132* (29), 10006−10008.

(15) Song, X.; Cheng, G.; Weber, D.; Pielnhofer, F.; Lei, S.; Klemenz, S.; Yeh, Y. W.; Filsinger, K. A.; Arnold, C. B.; Yao, N.; Schoop, L. M. Soft Chemical Synthesis of H_xCrS_2: An Antiferromagnetic Material with Alternating Amorphous and Crystalline Layers. *J. Am. Chem. Soc.* **2019**, *141* (39), 15634−15640.

(16) Yuan, F.; Song, X.; Cheng, G.; Yao, N.; Mozharivskyj, Y.; Schoop, L. M. Magnetic Nanosheets via Chemical Exfoliation of $K_{2-X}Mn_xSn_{1-X}S_2$. *Chem. Mater.* **2022**, *34* (11), 5084−5093.

(17) Wang, M.; Al-Dhahir, I.; Appiah, J.; Koski, K. J. Deintercalation of Zero-Valent Metals from Two-Dimensional Layered Chalcogenides. *Chem. Mater.* **2017**, *29* (4), 1650−1655.

(18) Uppuluri, R.; Sen Gupta, A.; Rosas, A. S.; Mallouk, T. E. Soft Chemistry of Ion-Exchangeable Layered Metal Oxides. *Chem. Soc. Rev.* **2018**, *47* (7), 2401−2430.

(19) Goodenough, J. B.; Park, K. S. The Li-Ion Rechargeable Battery: A Perspective. *J. Am. Chem. Soc.* **2013**, *135* (4), 1167−1176.

(20) Alameda, L. T.; Baumler, K. J.; Katzbaer, R. R.; Schaak, R. E. Soft Chemistry of Hard Materials: Low-Temperature Pathways to Bulk and Nanostructured Layered Metal Borides. *Acc. Chem. Res.* **2023**, *56* (23), 3515−3524.

(21) Cordova, D. L. M.; Johnson, D. C. Synthesis of Metastable Inorganic Solids with Extended Structures. *ChemPhysChem* **2020**, *21* (13), 1345−1368.

(22) Stein, A.; Keller, S. W.; Mallouk, T. E. Turning down the Heat: Design and Mechanism in Solid-State Synthesis. *Science (1979)* **1993**, *259* (5101), 1558−1564.

(23) Pati, S. K.; Rao, C. N. R. Kagome Network Compounds and Their Novel Magnetic Properties. *Chem. Commun.* **2008**, *39*, 4683−4693.

(24) Meschke, V.; Gorai, P.; Stevanović, V.; Toberer, E. S. Search and Structural Featurization of Magnetically Frustrated Kagome Lattices. *Chem. Mater.* **2021**, *33* (12), 4373−4381.

(25) Jovanovic, M.; Schoop, L. M. Simple Chemical Rules for Predicting Band Structures of Kagome Materials. *J. Am. Chem. Soc.* **2022**, *144* (24), 10978−10991.

(26) Wilson, S. D.; Ortiz, B. R. AV_3Sb_5 Kagome Superconductors. *Nat. Rev. Mater.* **2024**, *9*, 1−13.

(27) Chamorro, J. R.; McQueen, T. M.; Tran, T. T. Chemistry of Quantum Spin Liquids. *Chem. Rev.* **2021**, *121* (5), 2898−2934.

(28) Wang, Y.; Wu, H.; McCandless, G. T.; Chan, J. Y.; Ali, M. N. Quantum states and intertwining phases in kagome materials. *Nat. Rev. Phys.* **2023**, *5* (11), 635−658.

(29) Teng, X.; Oh, J. S.; Tan, H.; Chen, L.; Huang, J.; Gao, B.; Yin, J. X.; Chu, J. H.; Hashimoto, M.; Lu, D.; Jozwiak, C.; Bostwick, A.; Rotenberg, E.; Granroth, G. E.; Yan, B.; Birgeneau, R. J.; Dai, P.; Yi, M. Magnetism and Charge Density Wave Order in Kagome FeGe. *Nat. Phys.* **2023**, *19* (6), 814−822.

(30) Ye, L.; Kang, M.; Liu, J.; Von Cube, F.; Wicker, C. R.; Suzuki, T.; Jozwiak, C.; Bostwick, A.; Rotenberg, E.; Bell, D. C.; Fu, L.; Comin, R.; Checkelsky, J. G. Massive Dirac Fermions in a Ferromagnetic Kagome Metal. *Nature* **2018**, *555* (7698), 638−642.

(31) Neupert, T.; Denner, M. M.; Yin, J. X.; Thomale, R.; Hasan, M. Z. Charge Order and Superconductivity in Kagome Materials. *Nat. Phys.* **2022**, *18* (2), 137−143.

(32) Sinha, M.; Vivanco, H. K.; Wan, C.; Siegler, M. A.; Stewart, V. J.; Pogue, E. A.; Pressley, L. A.; Berry, T.; Wang, Z.; Johnson, I.; Chen, M.; Tran, T. T.; Phelan, W. A.; McQueen, T. M. Twisting of 2D Kagomé Sheets in Layered Intermetallics. *ACS Cent. Sci.* **2021**, *7* (8), 1381−1390.

(33) Arachchige, H. W. S.; Meier, W. R.; Marshall, M.; Matsuoka, T.; Xue, R.; McGuire, M. A.; Hermann, R. P.; Cao, H.; Mandrus, D. Charge Density Wave in Kagome Lattice Intermetallic ScV_6Sn_6. *Phys. Rev. Lett.* **2022**, *129* (21), No. 216402.

(34) Zhang, H.; Feng, H.; Xu, X.; Hao, W.; Du, Y. Recent Progress on 2D Kagome Magnets: Binary T_mSn_n (T = Fe, Co, Mn). *Adv. Quantum Technol.* **2021**, *4* (11), No. 2100073.

(35) Bronger, W.; Huster, J. $Cs_2Pd_3S_4$, Ein Neuer Schichtenstrukturtyp. *J. Less-Common Met.* **1971**, *23* (1), 67−72.

(36) Burschka, C. H. $CsCu_4S_3$ und $CsCu_3S_2$: Sulfide Mit Tetraedrisch Und Linear Koordiniertem Kupfer. *Z. Anorg. Allg. Chem.* **1980**, *463* (1), 65−71.

(37) Savelsberg, G.; Schäfer, H. Darstellung Und Kristallstruktur von $K_3Cu_3P_2$. *Z. fur Naturforsch., B: J. Chem. Sci.* **1978**, *33* (6), 590−592.

(38) Ortiz, B. R.; Gomes, L. C.; Morey, J. R.; Winiarski, M.; Bordelon, M.; Mangum, J. S.; Oswald, I. W. H.; Rodriguez-Rivera, J. A.; Neilson, J. R.; Wilson, S. D.; Ertekin, E.; McQueen, T. M.; Toberer, E. S. New Kagome Prototype Materials: Discovery of KV_3Sb_5, RbV_3Sb_5, and CsV_3Sb_5. *Phys. Rev. Mater.* **2019**, *3* (9), No. 094407.

(39) Mantravadi, A.; Gvozdetskyi, V.; Sarkar, A.; Mudryk, Y.; Zaikina, J. V. Exploring the A -V-Sb Landscape beyond AV_3Sb_5: A Case Study on the KV_6Sb_6 Kagome Compound. *Phys. Rev. Mater.* **2023**, *7* (11), No. 115002.

(40) Yang, Y.; Wang, R.; Shi, M. Z.; Wang, Z.; Xiang, Z.; Chen, X. H. Type-II Nodal Line Fermions in the Z2 Topological Semimetals AV_6Sb_6 (A = K, Rb, and Cs) with a Kagome Bilayer. *Phys. Rev. B* **2021**, *104* (24), No. 245128.

(41) Shi, M.; Yu, F.; Yang, Y.; Meng, F.; Lei, B.; Luo, Y.; Sun, Z.; He, J.; Wang, R.; Jiang, Z.; Liu, Z.; Shen, D.; Wu, T.; Wang, Z.; Xiang, Z.; Ying, J.; Chen, X. A New Class of Bilayer Kagome Lattice Compounds with Dirac Nodal Lines and Pressure-Induced Superconductivity. *Nat. Commun.* **2022**, *13* (1), 2773.

(42) Yang, Y.; Fan, W.; Zhang, Q.; Chen, Z.; Chen, X.; Ying, T.; Wu, X.; Yang, X.; Meng, F.; Li, G.; Li, S.; Gu, L.; Qian, T.; Schnyder, A. P.; Guo, J. G.; Chen, X. Discovery of Two Families of VSb-Based Compounds with V-Kagome Lattice. *Chin. Phys. Lett.* **2021**, *38* (12), No. 127102.

(43) Werhahn, D.; Ortiz, B. R.; Hay, A. K.; Wilson, S. D.; Seshadri, R.; Johrendt, D. The Kagomé Metals $RbTi_3Bi_5$ and $CsTi_3Bi_5$. *Z. Anorg. Allg. Chem.* **2022**, *77* (11−12), 757−764.

(44) Sun, Z.; Zhou, H.; Wang, C.; Kumar, S.; Geng, D.; Yue, S.; Han, X.; Haraguchi, Y.; Shimada, K.; Cheng, P.; Chen, L. Observation of topological flat bands in the kagome semiconductor Nb_3Cl_8. *Nano Lett.* **2022**, *22* (11), 4596−4602.

(45) Pasco, C. M.; El Baggari, I.; Bianco, E.; Kourkoutis, L. F.; McQueen, T. M. Tunable magnetic transition to a singlet ground state in a 2D van der Waals layered trimerized kagomé magnet. *ACS Nano* **2019**, *13* (8), 9457−9463.

(46) Manos, M. J.; Ding, N.; Kanatzidis, M. G. Layered Metal Sulfides: Exceptionally Selective Agents for Radioactive Strontium Removal. *Proc. Natl. Acad. Sci. U.S.A.* **2008**, *105* (10), 3696−3699.

(47) Kuonen, M.; Niu, G.; Hattendorf, B.; Günther, D. Characterizing a Nitrogen Microwave Inductively Coupled Atmospheric-Pressure Plasma Ion Source for Element Mass Spectrometry. *J. Anal. At. Spectrom.* **2023**, *38* (3), 758−765.

(48) Schild, M.; Gundlach-Graham, A.; Menon, A.; Jevtic, J.; Pikelja, V.; Tanner, M.; Hattendorf, B.; Günther, D. Replacing the Argon ICP: Nitrogen Microwave Inductively Coupled Atmospheric-Pressure Plasma (MICAP) for Mass Spectrometry. *Anal. Chem.* **2018**, *90* (22), 13443−13450.

(49) Mukta, S.; Gundlach-Graham, A. Ion Chromatography - Nitrogen-Sustained Microwave Inductively Coupled Atmospheric Pressure Plasma - Mass Spectrometry (IC-MICAP-MS) for Arsenic Speciation Analysis in Rice. *J. Anal. At. Spectrom.* **2024**, *39* (2), 491−499.

(50) Winckelmann, A.; Roik, J.; Recknagel, S.; Abad, C.; You, Z. Investigation of Matrix Effects in Nitrogen Microwave Inductively Coupled Atmospheric-Pressure Plasma Mass Spectrometry (MICAP-MS) for Trace Element Analysis in Steels. *J. Anal. At. Spectrom.* **2023**, *38* (6), 1253−1260.

(51) You, Z.; Akkuş, A.; Weisheit, W.; Giray, T.; Penk, S.; Buttler, S.; Recknagel, S.; Abad, C. Multielement Analysis in Soils Using Nitrogen Microwave Inductively Coupled Atmospheric-Pressure Plasma Mass Spectrometry. *J. Anal. At. Spectrom.* **2022**, *37* (12), 2556−2562.

(52) Juhás, P.; Davis, T.; Farrow, C. L.; Billinge, S. J. L. PDFgetX3: A Rapid and Highly Automatable Program for Processing Powder Diffraction Data into Total Scattering Pair Distribution Functions. *J. Appl. Crystallogr.* **2013**, *46* (2), 560−566.

(53) Farrow, C. L.; Juhas, P.; Liu, J. W.; Bryndin, D.; Boin, E. S.; Bloch, J.; Proffen, T.; Billinge, S. J. L. PDFfit2 and PDFgui: Computer Programs for Studying Nanostructure in Crystals. *J. Phys.: Condens. Matter* **2007**, *19* (33), No. 335219.

(54) Chupas, P. J.; Chapman, K. W.; Kurtz, C.; Hanson, J. C.; Lee, P. L.; Grey, C. P. A Versatile Sample-Environment Cell for Non-ambient X-Ray Scattering Experiments. *J. Appl. Crystallogr.* **2008**, *41* (4), 822−824.

(55) Blöchl, P. E. Projector Augmented-Wave Method. *Phys. Rev. B* **1994**, *50* (24), 17953.

(56) Kresse, G.; Furthmüller, J. Efficiency of Ab-Initio Total Energy Calculations for Metals and Semiconductors Using a Plane-Wave Basis Set. *Comput. Mater. Sci.* **1996**, *6* (1), 15−50.

(57) Kresse, G.; Furthmüller, J. Efficient Iterative Schemes for Ab Initio Total-Energy Calculations Using a Plane-Wave Basis Set. *Phys. Rev. B* **1996**, *54* (16), 11169.

(58) Perdew, J. P.; Burke, K.; Ernzerhof, M. Generalized Gradient Approximation Made Simple. *Phys. Rev. Lett.* **1996**, *77* (18), 3865.

(59) Baroni, S.; De Gironcoli, S.; Dal Corso, A.; Giannozzi, P. Phonons and Related Crystal Properties from Density-Functional Perturbation Theory. *Rev. Mod. Phys.* **2001**, *73* (2), 5151.

(60) Giannozzi, P.; Andreussi, O.; Brumme, T.; Bunau, O.; Buongiorno Nardelli, M.; Calandra, M.; Car, R.; Cavazzoni, C.; Ceresoli, D.; Cococcioni, M.; Colonna, N.; Carnimeo, I.; Dal Corso, A.; De Gironcoli, S.; Delugas, P.; Distasio, R. A.; Ferretti, A.; Floris, A.; Fratesi, G.; Fugallo, G.; Gebauer, R.; Gerstmann, U.; Giustino, F.; Gorni, T.; Jia, J.; Kawamura, M.; Ko, H. Y.; Kokalj, A.; Kücükbenli, E.; Lazzeri, M.; Marsili, M.; Marzari, N.; Mauri, F.; Nguyen, N. L.; Nguyen, H. V.; Otero-De-La-Roza, A.; Paulatto, L.; Poncé, S.; Rocca, D.; Sabatini, R.; Santra, B.; Schlipf, M.; Seitsonen, A. P.; Smogunov, A.; Timrov, I.; Thonhauser, T.; Umari, P.; Vast, N.; Wu, X.; Baroni, S. Advanced Capabilities for Materials Modelling with Quantum ESPRESSO. *J. Phys.: Condens. Matter* **2017**, *29* (46), No. 465901.

(61) Giannozzi, P.; Baseggio, O.; Bonfà, P.; Brunato, D.; Car, R.; Carnimeo, I.; Cavazzoni, C.; De Gironcoli, S.; Delugas, P.; Ferrari Ruffino, F.; Ferretti, A.; Marzari, N.; Timrov, I.; Urru, A.; Baroni, S. Quantum ESPRESSO toward the Exascale. *J. Chem. Phys.* **2020**, *152* (15), No. 154105.

(62) Bhaskar, G.; Gvozdetskyi, V.; Carnahan, S. L.; Wang, R.; Mantravadi, A.; Wu, X.; Ribeiro, R. A.; Huang, W.; Rossini, A. J.; Ho, K. M.; Canfield, P. C.; Lebedev, O. I.; Zaikina, J. V. Path Less

https://doi.org/10.1021/jacs.4c07285
J. Am. Chem. Soc. 2024, 146, 26786−26800

Traveled: A Contemporary Twist on Synthesis and Traditional Structure Solution of Metastable $LiNi_{12}B_8$. *ACS Mater. Au* **2022**, *2* (5), 614−625.
(63) Spek, A. L. Structure Validation in Chemical Crystallography. *Acta. Crystallogr. D Biol. Crystallogr.* **2009**, *65* (2), 148−155.
(64) Gvozdetskyi, V.; Sun, Y.; Zhao, X.; Bhaskar, G.; Carnahan, S. L.; Harmer, C. P.; Zhang, F.; Ribeiro, R. A.; Canfield, P. C.; Rossini, A. J.; Wang, C. Z.; Ho, K. M.; Zaikina, J. V. Lithium Nickel Borides: Evolution of [NiB] Layers Driven by Li Pressure. *Inorg. Chem. Front.* **2021**, *8* (7), 1675−1685.
(65) Chen, Z.; Beauvais, M. L.; Chapman, K. W. Pair Distribution Function Analysis of Discrete Nanomaterials in PDFgui. *J. Appl. Crystallogr.* **2023**, *56* (2), 328−337.
(66) Masadeh, A. S.; Božin, E. S.; Farrow, C. L.; Paglia, G.; Juhas, P.; Billinge, S. J. L.; Karkamkar, A.; Kanatzidis, M. G. Quantitative Size-Dependent Structure and Strain Determination of CdSe Nanoparticles Using Atomic Pair Distribution Function Analysis. *Phys. Rev. B* **2007**, *76* (11), No. 115413.
(67) Petkov, V.; Difrancesco, R. G.; Billinge, S. J. L.; Acharya, M.; Foley, H. C. Local Structure of Nanoporous Carbons. *Philos. Mag. B* **1999**, *79* (10), 1519−1530.
(68) Mills, A. M.; Mar, A. Layered Rare-Earth Gallium Antimonides $REGaSb_2$ (RE = La-Nd, Sm). *J. Am. Chem. Soc.* **2001**, *123* (6), 1151−1158.
(69) Chan, J. Y.; Wang, M. E.; Rehr, A.; Kauzlarich, S. M.; Webb, D. J. Synthesis, Structure, and Magnetic Properties of the Rare-Earth Zintl Compounds $Eu_{14}MnPn_{11}$ and $Eu_{14}InPn_{11}$ (Pn = Sb, Bi). *Chem. Mater.* **1997**, *9* (10), 2131−2138.
(70) Mantina, M.; Chamberlin, A. C.; Valero, R.; Cramer, C. J.; Truhlar, D. G. Consistent van Der Waals Radii for the Whole Main Group. *J. Phys. Chem. A* **2009**, *113* (19), 5806−5812.
(71) Van Der Batsanov, S. S. Waals Radii of Elements. *Inorg. Mater.* **2001**, *37* (9), 871−885.
(72) Frisenda, R.; Niu, Y.; Gant, P.; Muñoz, M.; Castellanos-Gomez, A. Naturally Occurring van Der Waals Materials. *npj 2D Mater. Appl.* **2020**, *4* (1), 38.
(73) Kauzlarich, S. M.; Brown, S. R.; Jeffrey Snyder, G. Zintl Phases for Thermoelectric Devices. *Dalton Trans.* **2007**, *21*, 2099−2107.
(74) Dolyniuk, J. A.; Owens-Baird, B.; Wang, J.; Zaikina, J. V.; Kovnir, K. Clathrate Thermoelectrics. *Mater. Sci. Eng., R* **2016**, *108*, 1−46.
(75) Stenger, V. A. Solubilities of Various Alkali Metal and Alkaline Earth Metal Compounds in Methanol. *J. Chem. Eng. Data* **1996**, *41* (5), 1111−1113.

https://doi.org/10.1021/jacs.4c07285
J. Am. Chem. Soc. 2024, 146, 26786−26800